# Electronic Supporting Information (ESI)

## Design of semitransparent tantalum nitride photoanode for efficient and durable solar water splitting

Tomohiro Higashi,*[a] Hiroshi Nishiyama,[b] Vikas Nandal,*[c] Yuriy Pihosh,[b] Yudai Kawase,[d] Ryota Shoji,[e] Mamiko Nakabayashi,[f] Yutaka Sasaki,[b] Naoya Shibata,[f] Hiroyuki Matsuzaki,[e] Kazuhiko Seki,[c] Kazuhiro Takanabe,[d] and Kazunari Domen*[b,g]

[a] Institute for Tenure Track Promotion, University of Miyazaki, Nishi 1-1 Gakuen-Kibanadai, Miyazaki, 889-2192, Japan
[b] Office of University Professors, The University of Tokyo, 2-11-16 Yayoi, Bunkyo-ku, Tokyo 113-8656, Japan
[c] Global Zero Emission Research Center, National Institute of Advanced Industrial Science and Technology, Tsukuba 16-1 Onogawa, Ibaraki 305-8569, Japan
[d] Department of Chemical System Engineering, School of Engineering, The University of Tokyo, 7-3-1 Hongo, Bunkyo-ku, Tokyo 113-8656, Japan
[e] Research Institute for Material and Chemical Measurement, National Metrology Institute of Japan (NMIJ), National Institute of Advanced Industrial Science and Technology, Tsukuba, 1-1-1 Higashi, Tsukuba, Ibaraki 305-8565, Japan
[f] Institute of Engineering Innovation, The University of Tokyo, 2-11-16 Yayoi, Bunkyo-ku, Tokyo, 113-8656, Japan
[g] Research Initiative for Supra-Materials (RISM), Shinshu University, 4-17-1 Wakasato, Nagano 380-8533, Japan

*E-mails: domen@chemsys.t.u-tokyo.ac.jp, t_higashi@cc.miyazaki-u.ac.jp, nk.nandal@aist.go.jp

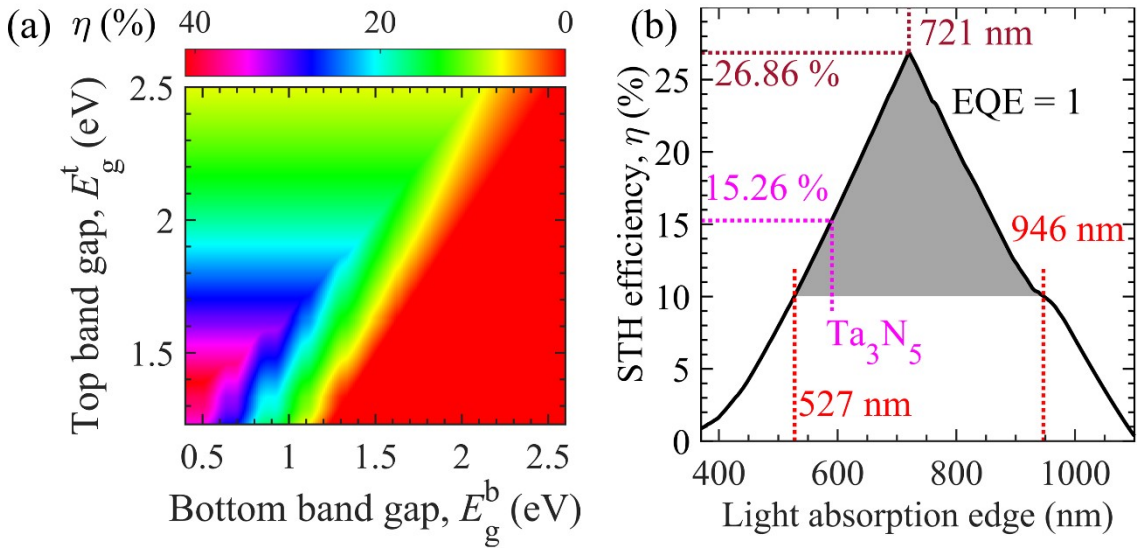


Figure S1. Theoretical limit of solar-to-hydrogen (STH) energy conversion efficiency $\eta$ for photoelectrochemical-photovoltaic tandem devices (a) against top $E_g^t$ and bottom energy band gap $E_g^b$ and (b) versus various light absorption edge (~ 1240/$E_g^t$) of top photo absorber semiconductor at $E_g^b$ of 1.12 eV. The current density in the top photo absorbing semiconductor is calculated by assuming external quantum efficiency (EQE) of 100% of the AM1.5G solar irradiance intensity above $E_g^t$. For bottom semiconductor, the current density is determined by assuming EQE of 100% of the transmitted light between $E_g^b$ and $E_g^t$. For tandem configuration with series connection of top and bottom semiconductors, the STH energy conversion efficiency is calculated by using the minimum of the current density extracted from top and bottom semiconductors $J$ by using $J \times 1.23$ V/$P_{in}$, where $P_{in}$ indicates the AM1.5G solar irradiance intensity. The top and bottom semiconductors produce current densities $J_t = q\int_{E_g^t}^{\infty} S(E)/E\, dE$ and $J_b = q\int_{E_g^b}^{E_g^t} S(E)/E\, dE$, respectively. Here, $S(E)$ is AM1.5G solar irradiation intensity in the units of W cm$^2$ eV$^{-1}$ at energy $E$ and q is the elemental charge.

**Table S1. Progress of photoelectrochemical-photovoltaic (PEC-PV) tandem devices for bias-free solar water splitting cell in the last decade.**

| Photoanode materials | Preparation methods | Co-catalyst | PV-cell | STH (%) | Year [ref] |
|---|---|---|---|---|---|
| Si-doped $Fe_2O_3$ | APCVD | $Co/Al_2O_3$ | DSSC | 1.17 | 2012 [1] |

| | | | | | |
|---|---|---|---|---|---|
| $Fe_2O_3$ | Hydrothermal | $NiFeO_x$ | Si | 0.91 | 2015 [2] |
| Si-doped $Fe_2O_3$ | APCVD | $NiFeO_x$ | PSC | 1.9 | 2015 [3] |
| Mn-doped $Fe_2O_3$ | Hydrothermal | $CoP_i$ | PSC | 2.4 | 2015 [4] |
| Sn-doped $Fe_2O_3$ | Hydrothermal | $CoP_i/SnO_x$ | PSC | 3.4 | 2017 [5] |
| (Ti,Si)-codoped $Fe_2O_3$ | Hydrothermal | $NiFeO_x$ | PSC | 4.49 | 2020 [6] |
| $WO_3$ | Sol-gel method | – | DSSC | 3.24 | 2011 [7] |
| $WO_3$ | Sol-gel method | – | DSSC | 3.1 | 2012 [1] |
| W-doped $BiVO_4$ | Spray pyrolysis | $CoP_i$ | Si | 4.9 | 2013 [8] |
| W-doped $BiVO_4$ | Spray pyrolysis | $CoP_i$ | Si | 5.2 | 2014 [9] |
| $BiVO_4$ | Electrodeposition | $CoB_i/TiO_2$ | Si | 3 | 2018 [10] |
| Dual-$BiVO_4$ | Electrodeposition | NiOOH/ FeOOH | PSC | 6.5 | 2018 [11] |
| $Ta_3N_5$ | Sputtering; nitridation | $NiFeO_x$ | CIS | 7.0 | 2019 [12] |
| Mg-doped $Ta_3N_5$ | Sputtering; nitridation | $NiFeO_x$ | ZnSe: CIGS | 0.05 | 2019 [13] |
| $Ta_3N_5$ | Sputtering; nitridation | $NiFeO_x$ | CIS | 9.0 | 2022 This work |

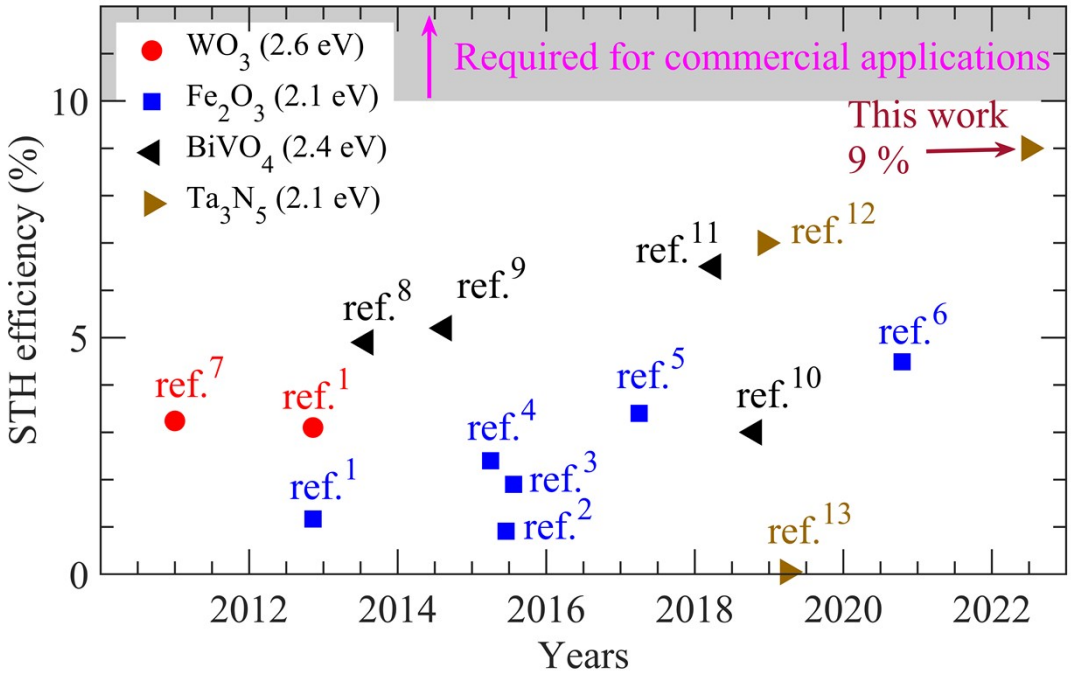


Figure S2. Evolution of solar-to-hydrogen (STH) energy conversion efficiency for different metal oxides/nitride based tandem technologies. The legends represent single

photo-absorber photoanode materials along with their typical bandgap energy. The details of respective tandem device are provided in Table S1, ESI.

**Table S2. Performance metrics of state-of-the-art wireless multijunction photoelectrochemical tandem devices for solar water splitting**

| Wireless monolithic systems | Electrocatalyst (cocatalyst) | STH, % | Durability, h | Electrolyte, pH | Year [ref] |
|---|---|---|---|---|---|
| 3-junction a-Si | Co-borate, NiMoZn | 2.5 | 10 | 1 M K-borate, pH 9.2 | 2011[14] |
| InGaP/GaAs | Ni/$TiO_2$, NiMo | 10.5 | 80 | 1 M KOH, pH 13.6 | 2015 [15] |
| $Al_xIn_{1-x}P$/ GaInP/GaInAs | $RuO_2$, Rh | 14 | 40 | 1 M $HClO_4$, pH 0 | 2015 [16] |
| InGaP/GaAs/Ge | $IrO_2$, Pt | 11.2 | 9 | 3 M $KHCO_3$ | 2017 [17] |
| GaInP/GaInAs, IMM-AlGaAs/GaInA | $IrO_x$, Pt | 16.2 | 1.5 | 3 M $H_2SO_4$, pH 1 | 2017 [18] |
| n-GaAs-Pt/Ti/Pt/Au/p-GaAs | $IrO_x$, Pt | 13.1 | 8 | 0.5 M $H_2SO_4$, pH 0.55 | 2017 [19] |
| GaAs/GaInAs/GaInP/AlInP/$TiO_2$ | $RuO_2$, Rh | 20 | 19.3 | 1 M $HClO_4$, pH 0 | 2018 [20] |
| GaAs/QW/GaInP | $IrO_x$, Pt/Ru | 13.6 | 2 (up to 10 h) | 0.5 M $H_2SO_4$ | 2019 [21] |
| GaAs/GaInAsP | $RuO_2$, $MoS_2$ | 6.1 | 12 | 0.5 M $H_2SO_4$ | 2020 [22] |

**Table S3. Performance metrics of state-of-the-art PEC-PV tandem devices based on PV grade (Si, chalcopyrite, PSC) materials for bias-free solar water splitting.**

| PEC-PV tandem system with photoanode/photocathode-PV | STH, % | Durability, h | Electrolyte, pH | Year [ref] |
|---|---|---|---|---|
| Pt/a-Si/a-Si photocathode and $RuO_2$ | 5.54 | - | 1 M $H_2SO_4$ | 2014 [23] |
| Pt/$TiO_2$/CdS/$CuIn_{1-x}Ga_xSe_2$ photocathode and $IrO_x$/lead halide PSC | 6.3 | 1 | 0.5 M $H_2SO_4$, pH 0 | 2015 [24] |
| $RuO_x$/$TiO_2$/Al:ZnO/$Cu_2O$/Au/ FTO photocathode and $IrO_x$/lead halide PSC | 2.5 | 2 | 0.5 M $K_2SO_4$, pH 5 | 2015 [25] |
| NiOOH/FeOOH/$BaSnO_3$ photoanode and Pt/PSC (using beam splitter) | 7.92 | 100 | 1 M Na-borate, pH 9.5 | 2019 [26] |

| | | | | |
|---|---|---|---|---|
| NiMo/2-jn Si-PV/Si-PC/Si-PA/Ni | 9.8 | 100 | 1 M KOH, pH 13.6 | 2019 [27] |
| Pt/Ti/P+nn+-Si photocathode and lead halide PSC | 17.6 | 72 | 1 M $H_2SO_4$ | 2020 [28] |
| Ni nanoparticles/$Ni(OH)_2$/n-Si and lead halide PSC | 12 | 140 | 1 M NaOH, pH 14 | 2020 [29] |

## 1. Materials and Methods

### 1.1. Preparation of planar $Ta_3N_5$ film on transparent $GaN/Al_2O_3$ substrate

The precursor of planar thin film of $Ta_3N_5$ was fabricated in a custom-made radio-frequency (RF) magnetron sputtering (RF-MS) system (ES-250L, Eiko), which was equipped with a function generator apparatus. The Si-doped n-type GaN layer (with thickness of 6 μm) coated on double-side-polished sapphire ($GaN/Al_2O_3$) plates (Powdec. Co., 10×15×0.65 mm) were used as the substrates to deposit $Ta_3N_5$ precursor films. $GaN/Al_2O_3$ substrates were located over the magnetron source of Ta metal disk [(purity 99.99 %), Kojundo Chem. Lab. Co.] with a diameter of 60 mm and thickness of 3 mm. Pre-sputtering of Ta target was performed in an Ar atmosphere for 10 minutes to clean its surface from contamination or impurities. The base pressure in the sputtering chamber was less than $2\times10^{-7}$ Pa, and the precursor films were deposited by sputtering process at high RF power of 200 W in 13.6 MHz for 2 hours. The RF input was turned on and off by the intermittent frequency of 1 kHz with a duty of 40 %. During the sputtering process, the working pressure of Ar gas atmosphere in the chamber was maintained at 3.13 Pa, which was monitored by a sapphire diaphragm gauge. The sputtering rate of Ta was adjusted to ~ 4.0 nm $min^{-1}$, which was equivalent to the previously reported conventional RF-MS at a relatively low RF power of 70 W.[12, 30-32] A schematic illustration of high and low RF power signals for sputtering is provided in Fig. S3, ESI. As a result, the precursor films with a thickness of ~ 600 nm were obtained. Following on, the samples were subjected to nitridation process at constant temperature of 1 hours in mixed $NH_3$ and $N_2$ gases with the respective flow rate of 120 sccm and 80 sccm. The temperature ramp rate of 10 K $min^{-1}$ was employed for nitridation process following by natural cooling at the same gases conditions. Consequently, the nitridation process produced planar films of $Ta_3N_5$ with the thickness ~ 800 nm. The additional details of the input RF power for sputtering and nitridation process are provided in Figs. S3 and S5a.

### 1.2. Surface modification of $Ta_3N_5$ by $NiFeO_x$ electrocatalyst

The depositions of $NiFeO_x$ electrocatalyst on the surface of $Ta_3N_5/GaN/Al_2O_3$ was done by using drop-casting[12] and spin-coating methods[32]. The precursor solution for $NiFeO_x$ was prepared by dissolving iron (III) 2-ethylhexanoate (Wako) and nickel (II) 2-ethyl hexanoate (Wako) in hexane (HPLC grade, Wako) and toluene (>99.5 %, Sigma-Aldrich). For the drop-casting method, 10 μL of iron (III) 2-ethylhexanoate and 10 μL of nickel (II) 2-ethyl hexanoate (8.7 μmol of Fe complex + 8.9 μmol of Ni complex) were mixed in 10 mL of hexane. This solution with the amount of 100 μL was drop casted on the $Ta_3N_5$ surface (sample area of ~ 0.8-0.9 $cm^2$). The precursor loaded specimen was heated at temperature of 413 K for 1 hour in the air for the removal of the residual hexane from the $Ta_3N_5$ surface. The calculated amount of $NiFeO_x$ loaded on $Ta_3N_5$ surface was 0.1 μmol $cm^{-2}$.[32] For the spin-coating method, 500 μL of iron (III) 2-ethylhexanoate and 500 μL of nickel (II) 2-ethylhexanoate (435 μmol of Fe complex + 445 μmol of Ni complex) were dissolved in 3 mL of toluene, which was spin coated on $Ta_3N_5$ surface (sample area of ~ 0.8-0.9 $cm^2$) under sample rotation speed of 5000 rpm for 60 seconds. Further, the spin coated samples were heated at temperature of 413 K for 1 hour in the air to remove residues of toluene. A summary of drop-casting and spin-coating methods for the deposition of $NiFeO_x$ electrocatalyst on $Ta_3N_5$ surface is provided in Figs. S5b and S5c.

### 1.3. Characterization

The fabricated $Ta_3N_5$ film on $GaN/Al_2O_3$ substrates were characterized by different techniques, such as: X-ray diffraction (XRD; Smart Lab, Rigaku), Hall effect measurements (Model 8404, Lake Shore) using Van der Pauw method, UV-Vis transmission/reflection spectroscopy (V-670, JASCO), scanning electron microscopy (SEM; SU8020, Hitachi), scanning transmission electron microscopy (STEM; JEM-2800, JEOL), and transmission electron microscopy (TEM; JEM-2800, JEOL). The TEM was equipped with selected-area electron diffraction (SAED) and energy dispersive X-ray spectroscopy (EDS) capabilities. The surface chemical stats of the samples were characterized by X-ray photoelectron spectroscopy (XPS) (ULTRA2, KRATOS). The binding energy of the obtained XPS spectra was calibrated to the C1s peak of carbon at 284.4 eV.

### 1.4. Photoelectrochemical (PEC) measurements

Prior to PEC measurements, the indium metal was soldered on the part of GaN to form an ohmic contact, and then lead wire was connected using additional indium solder. The

bare indium and exposed part of GaN were covered with epoxy resin for insulation. The PEC measurements were carried out in a three-electrode configuration. The working electrode, the reference electrode, and the counter electrode were $Ta_3N_5$ photoanode, Ag/AgCl/sat'd KCl ($E_{Ag/AgCl/sat'd\ KCl}$ = 0.197 V vs. Normal hydrogen electrode at 25°C), and coiled-Pt wire, respectively. These three-electrodes were immersed into 1 M KOH aqueous based electrolyte of pH 13.8 inside of PEC glass cell. The potentiostat (HV-110, Hokuto Denko) was employed to control the electrode potential of $Ta_3N_5$ photoanode. The schematic illustration and photograph of the $NiFeO_x/Ta_3N_5/GaN$ photoanode and the PEC measurement in three-electrode configuration are provided in Fig. S10. The electrode potential was referred to a reversible hydrogen electrode (vs. RHE), as per the Nernst equation below:

$$E_{\text{vs. RHE}} = E_{\text{vs. Ag/AgCl/sat'd KCl}} + E_{Ag/AgCl/sat'd\ KCl} + 0.059\text{pH}. \quad \text{(S1)}$$

A solar simulator (XES-40S2, SAN-EI Electric. Co. Ltd) equipped with AM 1.5G filter was utilized as the light source. The intensity of the incident light was calibrated to 100 mW $cm^{-2}$ (corresponding to AM 1.5G, 1 sun) using an LS-100 spectroradiometer (EKO Instrument). The measured current at different potentials (with scan rate of 10 mV $s^{-1}$) was normalized with the photoactive area (~ 0.8-0.9 $cm^2$) to determine the current density $J$ of the photoanode under dark and simulated AM1.5G solar illumination conditions. The half-cell solar-to-hydrogen (HC-STH) energy conversion efficiency $\eta$ of $NiFeO_x/Ta_3N_5/GaN/Al_2O_3$ photoanodes were estimated from the measured current density-potential ($J$-$E$) curves by using:

$$\eta\,(\%) = J \times (E^{o}_{O_2/H_2O} - E) \times 100 / P_{in}\,, \quad \text{(S2)}$$

where, $E$ is the applied potential in RHE scale, $E^{o}_{O_2/H_2O}$ (1.23 V) is the standard redox potential of water for OER, and $P_{in}$ (100 mW $cm^{-2}$) is the power of the incident AM1.5 solar spectrum. Furthermore, the ratio-metric power-saved figure of merit (FOM) of the photoanode was calculated and given by:

$$\text{FOM}\,(\%) = J \times (E_J - E) \times 100 / P_{in}\,. \quad \text{(S3)}$$

Here, $E_J$ is the electrode potential of electrocatalyst generating the current equivalent to $J$. The $J$ and $E_J$ were determined from $J$-$E$ curves of $NiFeO_x/Ta_3N_5/GaN/Al_2O_3$ photoanode and $NiFeO_x$ electrocatalyst loaded on Au-coated Ti electrode, respectively.

The incident photon-to-current efficiency (IPCE) was measured by MAX-302 Xe light source (Asahi spectra), which was equipped with bandpass filters to generate monochromatic light. The IPCE spectra was determined by the following relation:

$$\text{IPCE}\,(\%) = [(1240 / \lambda) \times J / P] \times 100. \quad \text{(S4)}$$

Here, $\lambda$ (nm) is the wavelength of the monochromatic incident light, $J$ is the photocurrent density (mA $cm^{-2}$) and $P$ (mW $cm^{-2}$) is the power of the monochromatic light.

Electrochemical impedance spectroscopy (EIS) (using SP-300 Potentiostat-Biologic equipment) of the semitransparent photoanodes was performed at a potential of 1.23 $V_{RHE}$ with an AC amplitude of 10 mV and frequencies ranging from 0.1 Hz to 100 kHz.

### 1.5. Electrochemical measurements for $NiFeO_x$ electrocatalyst

To evaluate the electrochemical properties of $NiFeO_x$ electrocatalyst for OER, the $NiFeO_x$ electrocatalyst was deposited on the Au-coated Ti foil (Au/Ti). Initially, the Au layer with a thickness of 2 μm was coated on the 50 μm thick Ti foil (10×10 mm) by RF magnetron sputtering. $NiFeO_x$ electrocatalyst was deposited on the Au/Ti specimen by using similar protocols (drop casting and spin coating), which were employed for the preparation of $NiFeO_x/Ta_3N_5/GaN/Al_2O_3$ photoanode. The $NiFeO_x$-modified Au/Ti samples are abbreviated as $NiFeO_x$/Au/Ti electrodes. The electrochemical properties such as overpotential and onset potential of $NiFeO_x$/Au/Ti electrodes for OER were assessed by cyclic voltammetry (CV) and chronoamperometry (CA) with Hg/HgO (1 M NaOH) reference electrode and Pt-wire counter electrode. The CV and CA were acquired in 1 M KOH aqueous solution with pH 13.9, under Ar gas atmosphere and dark condition.

### 1.6. Overall water splitting by the tandem cell

Multi-stage series-connected $CuInSe_2$ (CIS)-based thin-film solar cells prepared by Solar Frontier K.K. were employed to fabricate a two series-connected (dual-) CIS unit terminated with a Pt/Ni plate electrode (abbreviated as Pt/Ni/dual-CIS electrode). For this, the electrical contact between the dual-CIS unit and Pt/Ni plate was provided by indium tin oxide (ITO) and carbon housing, as per previous work reported in the literature.[12] The $NiFeO_x/Ta_3N_5/GaN/Al_2O_3$ photoanode (placed in front) was wired in series with Pt/Ni/dual-CIS electrode to construct a tandem cell. This tandem configuration allowed the simulated sunlight at the wavelengths shorter than 600 nm to be absorbed by the $Ta_3N_5$, while the transmitted spectrum (longer than 600 nm) was absorbed up to wavelength of 1100 nm by the dual-CIS unit. The $NiFeO_x/Ta_3N_5/GaN/Al_2O_3$ semitransparent photoanode and the Pt/Ni/dual-CIS electrode were connected to a multimeter through lead wires, and the photocurrent generated in response to simulated sunlight was monitored to determine the STH energy conversion efficiency for overall water splitting (OWS) reaction in 1 M KOH aqueous solution (pH = 13.8). The STH energy conversion efficiency of the tandem cell was calculated from the evolution of the current density $J$ with time $t$ ($J$-$t$ characteristics), as per following equation:

$$\text{STH}\ (\%) = J \times 1.23\ \text{V} \times 100 / P_{\text{in}}. \quad \text{(S5)}$$

Here, the *J* was estimated by normalizing the bias-free measured current (in response to solar energy only) with the photoactive area (0.8-0.9 $cm^2$) of the photoanode.

### 1.7. Theoretical analysis of the degradation of $NiFeO_x$ electrocatalyst

In $NiFeO_x$/Au/Ti electrodes, the degradation in current could originate from the loss of OER-active Fe species from $NiFeO_x$, which gets dissolved into the electrolyte solution as a most likely $FeO_4^{2-}$ species. We theoretically study the current density $J(t)$ as a function of time $t$ by taking into account the dissolution of Fe species. Below, we call $NiFeO_x$-loaded surface retaining OER-active Fe species as the active $NiFeO_x$. The fraction of active $NiFeO_x$ $f(t)$ decreases with time as

$$\frac{d}{dt}f(t) = -k_{\mathrm{diss}}J(t)f, \qquad (S6)$$

where $J(t)$ indicates the current density and $k_{\mathrm{diss}}$ is the dissolution rate constant. The resistance of $NiFeO_x$ electrocatalyst is denoted by $R_{\mathrm{c}} = \rho_{\mathrm{c}} l/S(t)$, where $\rho_{\mathrm{c}}$, $l$, and $S(t)$ indicate the electrical resistivity, depth and the surface area of the active $NiFeO_x$ electrocatalyst. By denoting the initial surface area by $S_0$, we define $f(t) = S(t)/S_0$. The resistance of active $NiFeO_x$ electrocatalyst can be expressed as $R_{\mathrm{c}}(t) = r_{\mathrm{ci}}/S(t)$, where $r_{\mathrm{ci}} = \rho_{\mathrm{c}} l$ and $r_{\mathrm{ci}}/S_0$ is the initial resistance of active $NiFeO_x$ electrocatalyst.

We introduce the resistance of degraded $NiFeO_x$ electrocatalyst caused by the dissolution of the active Fe species into the electrolyte solution. The surface area of the degraded $NiFeO_x$ is $S_d(t) = S_0(1 - f(t))$ and the resistance of degraded $NiFeO_x$ is given by $R_{\mathrm{d}}(t) = \rho_{\mathrm{d}} l/S_d(t)$, where $\rho_{\mathrm{d}}$ is the resistivity of the degraded $NiFeO_x$. The resistance of degraded $NiFeO_x$ electrocatalyst can be expressed as $R_{\mathrm{d}}(t) = r_{\mathrm{df}}/S_d(t)$, where $r_{\mathrm{df}} = \rho_{\mathrm{d}} l$ and $r_{\mathrm{df}}/S_0$ is the final resistance of $NiFeO_x$ electrocatalyst degraded by dissolution of OER-active Fe species.

The coexistence of the active $NiFeO_x$ electrocatalyst and the degraded $NiFeO_x$ electrocatalyst can be regarded as electrically parallel connection to a voltage; the voltage which drives the current is the excess potential $\Delta V$ given by the difference between the measured voltage $V_J$ at current density $J$ and $V_{J=0}$ which is the maximum voltage obtained under negligibly small current density (In this manuscript 0.1 mA $cm^{-2}$ and 1.48 $V_{\mathrm{RHE}}$), $\Delta V = V_J - V_{J=0}$. The electrical current density under the excess potential $\Delta V$ can be

expressed as

$$J(t)S_0 = \left(\frac{1}{R_c(t)} + \frac{1}{R_d(t)}\right)\Delta V. \qquad (S7)$$

By substituting $R_c(t) = r_{ci}/S(t)$ and $R_d(t) = r_{df}/S_d(t)$, Eq. S7 can be rewritten as

$$J(t) = \left(\frac{f(t)}{r_{ci}} + \frac{1-f(t)}{r_{df}}\right)\Delta V. \qquad (S8)$$

By rearrangement, we find

$$f(t) = \frac{J(t)/\Delta V - 1/r_{df}}{1/r_{ci} - 1/r_{df}}. \qquad (S9)$$

By time differentiation of Eq. S9, we obtain

$$\frac{d}{dt}f(t) = \left(\frac{1}{r_{ci}} - \frac{1}{r_{df}}\right)^{-1}\frac{1}{\Delta V}\frac{d}{dt}J(t). \qquad (S10)$$

By substituting Eqs. S9 and S10, Eq. S6 becomes a closed equation for $J(t)$ as

$$\frac{d}{dt}J(t) = -k_{diss}J(t)\left(J - \frac{\Delta V}{r_{df}}\right). \qquad (S11)$$

The solution can be expressed as

$$\frac{J_0}{J(t)} = \frac{r_{df}}{r_{ci}} - \left(\frac{r_{df}}{r_{ci}} - 1\right)\exp\left(-k_{diss}J_0\frac{r_{ci}}{r_{df}}t\right), \qquad (S12)$$

where $J_0$ is the initial current density and satisfies $J_0 = \Delta V/r_{ci}$.

In Fig. S17, the experimental data of $J_0/J(t)$ are fitted to Eq. S12. We find that the $k_{diss}$ value is 1.3 times higher for the spin-coating method compared to the drop-casting method. The $r_{df}$ value is 1.6 times higher for the spin-coating method compared to the drop-casting method.

### 1.8. Photoluminescence (PL) measurements

Picosecond time-resolved PL measurements were carried out using a streak camera (Hamamatsu Photonics, StreakScope C4334) equipped with a monochromator to detect the PL spectra of $Ta_3N_5/GaN/Al_2O_3$ sample fabricated by high input power RF-MS. The thickness of $Ta_3N_5$ layer is about 850 nm. A Ti: sapphire laser with a regenerative amplifier (Spectra-Physics, Solstice, wavelength of 800 nm, pulse width of 100 fs, pulse

energy of 3.5 mJ per pulse and repetition rate of 1 kHz) was employed as a light source. The second-harmonic light (400 nm) generated from the fundamental light (800 nm) by using β-$BaB_2O_4$ crystal was used for the excitation light. The excitation light was irradiated from $Ta_3N_5$ layer side.

### 1.9. Transient absorption spectroscopy (TAS) measurements

In the TAS measurements, TA signal is presented herein in units of percentage absorption (Absorption (%)), calculated as $100\times(1 - T/T_0)$, where $T$ and $T_0$ are the intensities of the transmitted probe light passing through sample with and without pump excitation, respectively. The measured $Ta_3N_5$/GaN/$Al_2O_3$ sample was identical to that in the PL measurements described above. Femtosecond TAS measurements ($t < 3$ ns) were carried out using a Ti: sapphire laser with a regenerative amplifier (Spectra-Physics, Solstice, wavelength of 800 nm, pulse width of 100 fs, pulse energy of 3.5 mJ per pulse and repetition rate of 1 kHz) as a light source. The output from the laser was split into four paths for the excitation of two optical parametric amplifiers (OPAs: Spectra-Physics, TOPAS Prime), the white-light-continuum generation by focusing the fundamental light (800 nm) into a sapphire plate, and the second- and third-harmonic generations of the fundamental light (800 nm) by using BBO (β-$BaB_2O_4$) crystals. The second-harmonic light (400 nm) was used for pump light, and pump light intensity was varied by neutral density filters from 0.075 μJ/pulse to 4.5 μJ/pulse. For the probe light, infrared (IR) light of 5120 nm (0.24 eV) generated from OPA equipped with difference-frequency generation crystal was used. The delay time of the probe pulse relative to the pump pulse was controlled up to 3 ns by changing the optical path length of the pump pulse. The time resolution of the system was about 140 fs. A liquid-nitrogen-cooled HgCdTe photodetector (Kolmar Technologies, KMPV11-1-J1) was used to detect the transmitted probe light passing through $Ta_3N_5$/GaN/$Al_2O_3$. Both pump and probe lights were irradiated from $Ta_3N_5$ layer side. The diameter of the pump beam on the sample was about 1 mm and the irradiated area of the pump beam was evaluated using a beam profiler (Newport LBP2-HR-VIS2).

In TAS measurements for $t > 3$ ns, the continuous-wave IR light of 5250 nm (0.24 eV) from a quantum cascade laser (Thorlabs, QD5250CM1 AB152) was used as the probe light source. The pump light of 400 nm was identical to that used in the measurements for $t < 3$ ns described above. The transmitted probe light passing through $Ta_3N_5$/GaN/$Al_2O_3$ was detected by a liquid-nitrogen-cooled fast HgCdTe photodetector (Kolmar Technologies, KV104-0.25-A-2/11, bandwidth of 80 MHz). The signal from the detector was amplified with a voltage amplifier (Femto, DHPVA-200) and subsequently

processed and recorded with a digital oscilloscope (Lecroy, WaveRunner 6200 A). The pump-induced signal (AC signal) was selectively extracted by using the AC-coupled mode of the amplifier. The DC offset of the signal from the detector, on the other hand, was independently recorded with a digital multimeter (National Instruments, USB-4065) to calculate the Absorption (%). As a result, very small TA signals (<0.01 %) were detected with few ns time resolution.

### 1.10. Theoretical model formulation for charge carrier dynamics

Figure 5c shows the governing relaxation processes of charge carriers behind absorption signal decay characteristics of $Ta_3N_5$ thin film, prepared by high RF power sputtering technique. Under pump photon excitation, the excess electron $\Delta n_0$ and hole density $\Delta p_0$ are generated inside conduction $E_c$ and valence energy bands $E_v$ of $Ta_3N_5$ thin film. These initial densities of photogenerated charge carriers ($\Delta n_0$; $\Delta p_0$) are equal and rise linearly with the increase of photon flux density $I_p$ and pump fluence intensity $P_{FL}$, as evident from Fig. S23. With absorption coefficient $\alpha_a$ = 2.91 × $10^5$ $cm^{-1}$ (from ellipsometry measurement) at pump photon excitation energy of 3.1 V, the $\Delta n_0$ is regulated in the range of 4.7 × $10^{18}$ $cm^{-3}$ to 2.82 × $10^{20}$ $cm^{-3}$ by the modulation of $P_{FL}$ from 0.075 μJ per pulse to 4.5 μJ per pulse, as per Lambert-Beer law. Besides $\Delta n_0$, the $E_c$ contains equilibrium or dark electron density $n_d$, which is typically reported of the order of $10^{19}$ $cm^{-3}$ from Hall effect measurements/Mott-Schottky analysis[12]. With probe photon energy of 0.24 eV, the maximum absorption signal $S_m$, at time $t$ = 0.4 ps, is proportional to the photogenerated charge carrier density *e.g.*, $S_m = \beta \Delta n_0$ with $\beta$ as the proportionality constant. After $t$ = 0.4 ps, the mobile holes are annihilated by band-to-band (or bimolecular) recombination with electrons at rate constant $k_r$. In addition, the mobile holes are trapped to exponential tail trap states of valence band at rate constant $k_t$. The energetic distribution of these trap states with density $N_t$ is defined by $N_t g(E)$ such that $g(E) = \exp(-E/E_0)/E_0$ and $\int g(E)dE = 1$. Here, $E_0$ is the characteristic energy (determined from exponent $\alpha$, inset of Fig. 5d) and $E$ is the energy with respect to $E_v$ (= 0 eV). Moreover, the accumulated holes in trap states are de-trapped to valence energy band with rate constant $k_d$. Under the detailed balance condition, $k_d = k_t \exp(-E/k_B T)$, where $k_B$ and $T$ are the Boltzmann constant and temperature, respectively. Based on above-mentioned processes, the dynamics of excess mobile electron density $\Delta n(t)$, mobile hole density $\Delta p(t)$, and trapped hole density $p_t(E, t)$ with time $t$ and energy $E$ is numerically simulated (using MATLAB) by the following Eqs. (S13-S15):

$$d\Delta n(t)/dt = - k_r \Delta p(t)[n_d + \Delta n(t)] \quad \text{(S13)}$$

$$d\Delta p(t)/dt = -k_r[n_d + \Delta n(t)]\Delta p(t) - k_t[N_t - p_t(t)]\Delta p(t) + \int k_d p_t(E,t)][N_v - \Delta p(t)]dE \quad (S14)$$

$$dp_t(E,t)/dt = k_t[N_t g(E) - p_t(E,t)]\Delta p(t) - k_d p_t(E,t)][N_v - \Delta p(t)] \quad (S15)$$

Here, $N_v$ is the effective density of states for valence energy band. Using trapezoidal method, the time evolution of total trapped density $p_t(t)$ is calculated by the integration $p_t(E,t)$ across energy $E$, *i.e.*, $p_t(t) = \int p_t(E,t)dE$. In Fig 5e and Fig. S24, the numerical simulation results corroborate well with the measured absorption signal decay dynamics. Table S4 provides the estimated/employed material parameters to simulate the charge carrier dynamics of $Ta_3N_5$ thin film.

### 1.11. Optical simulations

Optical simulations were performed to simulate the light absorption, reflection, and transmission of $Ta_3N_5$/GaN photoanode. Under normal operating conditions, the simulated AM1.5G solar light transmits from air through glass and water to illuminate $Ta_3N_5$ photoanode. Therefore, the optical model constitutes glass/water/$Ta_3N_5$/GaN, where the $Ta_3N_5$ and GaN thickness are fixed to 800 nm and 4 μm (confirmed by SEM image), respectively. The phase elimination method was employed to model water and glass media thickness to 300 nm - $\lambda/4n_r$.[33] Here, $\lambda$ is the wavelength and $n_r$ is the refractive index of water (1.33) and glass (1.47). Owing to 100 % light transparency, the extinction coefficient $k_e$ of glass and water are set to zero. Besides, Fig. S25 provides the $n_r$ and $k_e$ for $Ta_3N_5$ and GaN, which are utilized as material parameters for optical simulations. Using optics module of COMSOL Multiphysics, a linearly polarized light with power 1 W and wavelength $\lambda$ is incident at the air/glass interface of the modeled device (glass/water/$Ta_3N_5$/GaN). The device is well-discretized with the fine element size by using in-built physics-controlled meshing algorithm. A periodic boundary condition for continuous electric field is employed at the opposite sides of respective layers. The electromagnetic waves, frequency domain solves the Maxwell's equations to simulate the propagation of light/electric field at each discretized node across the device. Consequently, the light absorption (Abs), reflection (RF), and transmission (TR) spectra against wavelength $\lambda$ is determined in Fig. 6a. These optical spectra lead to integrated current density of 9.27 mA $cm^{-2}$ (as shown in Fig. 6b). Using Lambert-Beer law, in Fig. 6c, the generation rate $G$ of charge carriers under steady state AM1.5G solar irradiance inside $Ta_3N_5$ layer is calculated by the following equation:

$$G = c_0 \int \mathrm{Abs}(\lambda)\alpha_a(\lambda)N(\lambda)\exp(-\alpha_a(\lambda)x)\mathrm{d}\lambda \,. \quad \text{(S16)}$$

Here, $\alpha_a(\lambda) = 4\pi k_e/\lambda$ is the absorption coefficient, $N(\lambda)$ is the photon density of AM1.5G solar spectrum, $x$ is the position co-ordinate with respect to water/$Ta_3N_5$ interface, and $c_0$ = 1.04 is empirical scaling constant such that current density evaluated from generation rate and light absorption (Abs) are equal. The upper and lower limits for wavelength in Eq. S16 are 280 nm and 600 nm (absorption edge of $Ta_3N_5$), respectively. The calculated $G$ is used for electrical simulations of $Ta_3N_5$ photoanode.

### 1.12. Electrical simulations

Electrical simulations were carried out to determine performance affecting parameters of $Ta_3N_5$ photoanode. For this, an effective band model including shallow tail-states of $Ta_3N_5$ is employed, which is interfaced with ohmic back contact for electron extraction. Considering large valence band offset at the interface of GaN and $Ta_3N_5$, the hole extraction rate is zero. The $NeFeO_x$ electrocatalyst and water on the $Ta_3N_5$ surface is modelled as pseudo-metal contact. The work function of pseudo-metal contact is adjusted to the middle of water redox potential (4.28 eV, as per Nernst equation at pH 13.8), whereas the hole $S_h$ and electron extraction rate $S_n$ (dictated by $NeFeO_x$ electrocatalyst) are non-zero and zero, respectively. Under steady state AM1.5G solar illumination, the previously simulated generation rate $G$ produce free/mobile charge carriers inside respective conduction and valence energy bands. As evident from TAS analysis (Fig. 5), the charge carriers are subjected to direct band-to-band or bimolecular recombination with rate constant $k_r$. In addition, the $Ta_3N_5$ layer exhibited an n-type doping density $n_d$ as evaluated from charge carrier dynamics analysis. With fixed electron mobility of 2.72 $cm^2V^{-1}s^{-1}$ (from Hall effect measurement), the unknown hole mobility is varied from 10 $cm^2V^{-1}s^{-1}$ to $10^5$ $cm^2V^{-1}s^{-1}$ for tuning the hole diffusion length in the range from 18 nm to 570 nm at carrier lifetime ($1/(k_r n_d)$) of 12.5 ps. To reduced simulation cost, one-dimensional model is utilized and well-discretized to simulate sharp energy band bending in space charge/depletion region at water/$Ta_3N_5$ interface. With semiconductor module of COMSOL Multiphysics, the governing semiconductor equations *i.e.,* Poisson, continuity, and drift-diffusion equations for electrons and holes[34] are solved self-consistently at each discretized node for various applied potential $V_a$ at the back GaN contact. Here, the $V_a$ is scaled to potential $E$ in RHE scale, which is incorporated with the series resistance $R_s$ effect. Accordingly, the $E = (V_a + V_{RO}/2) + JR_s$, where $V_{RO}$ (= 1.23 V) and $J$ are the water redox potential and simulated current density. Consequently, the trends of current at 1.23 $V_{RHE}$ against hole diffusion length in Fig. 6c and current-potential

(*J-E*) curve in Fig. 6d are simulated. Table S5 provides the extracted material parameters ($S_h$; $R_s$; $L_{dh}$) of the calibrated model of $Ta_3N_5$ photoanode.

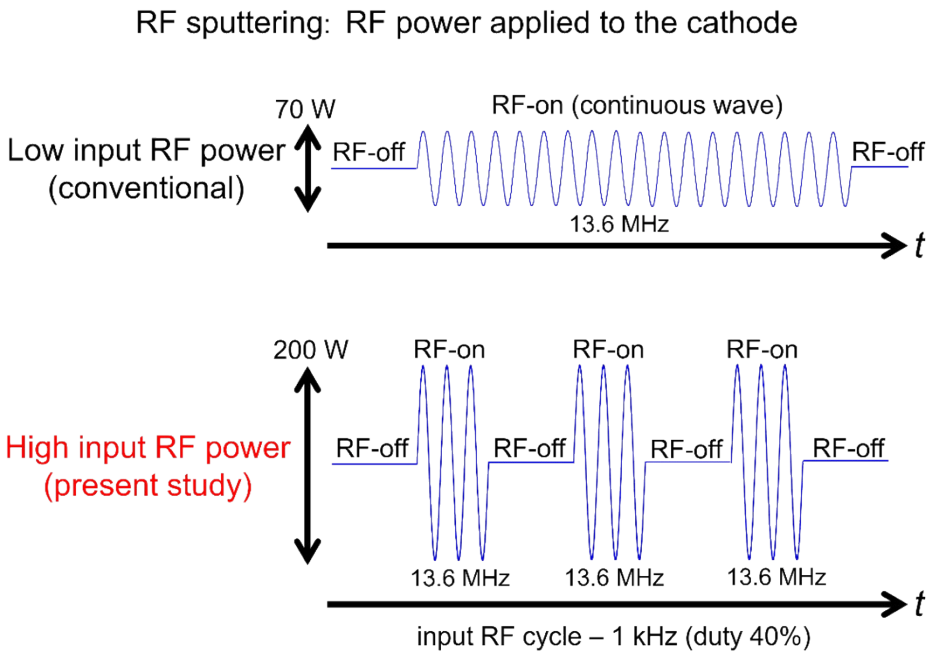


Figure S3. Schematic illustration of low and high input power radio-frequency magnetron sputtering (RF-MS).

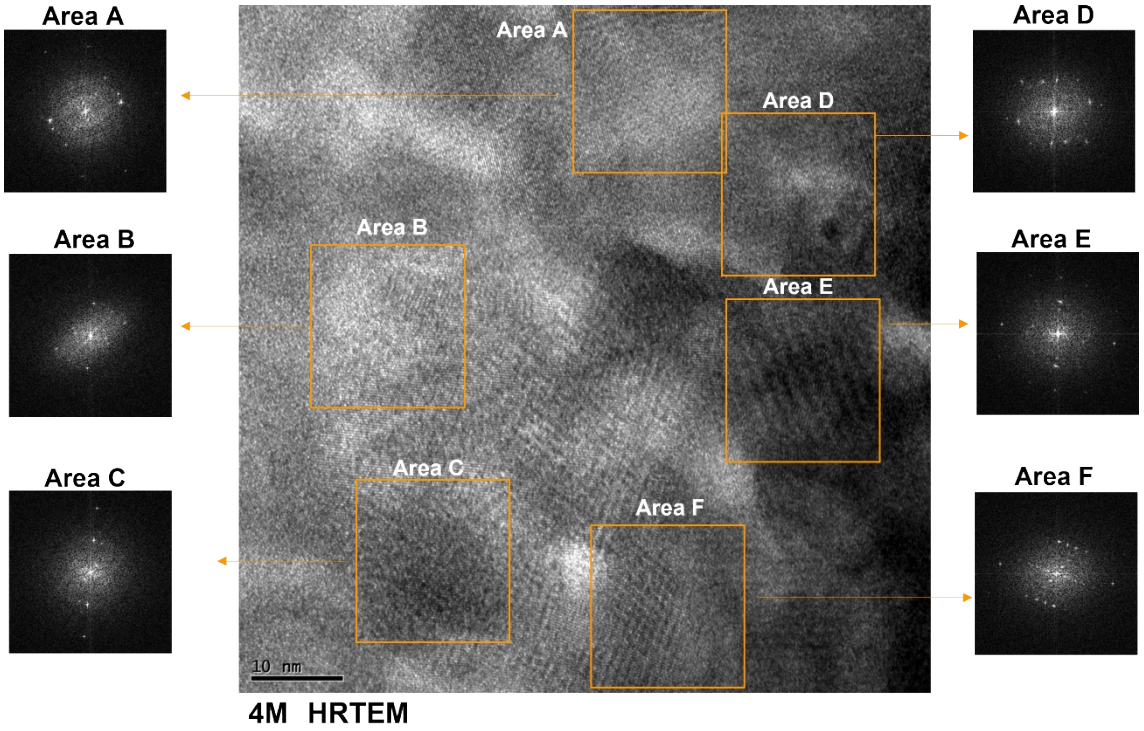


Figure S4. High-resolution transmission electron microscopy (HRTEM) image of $Ta_3N_5$ surface. Corresponding fast Fourier transforms (FFT) in several specified areas (A-F) on the surface of $Ta_3N_5/GaN/Al_2O_3$ specimen are shown.

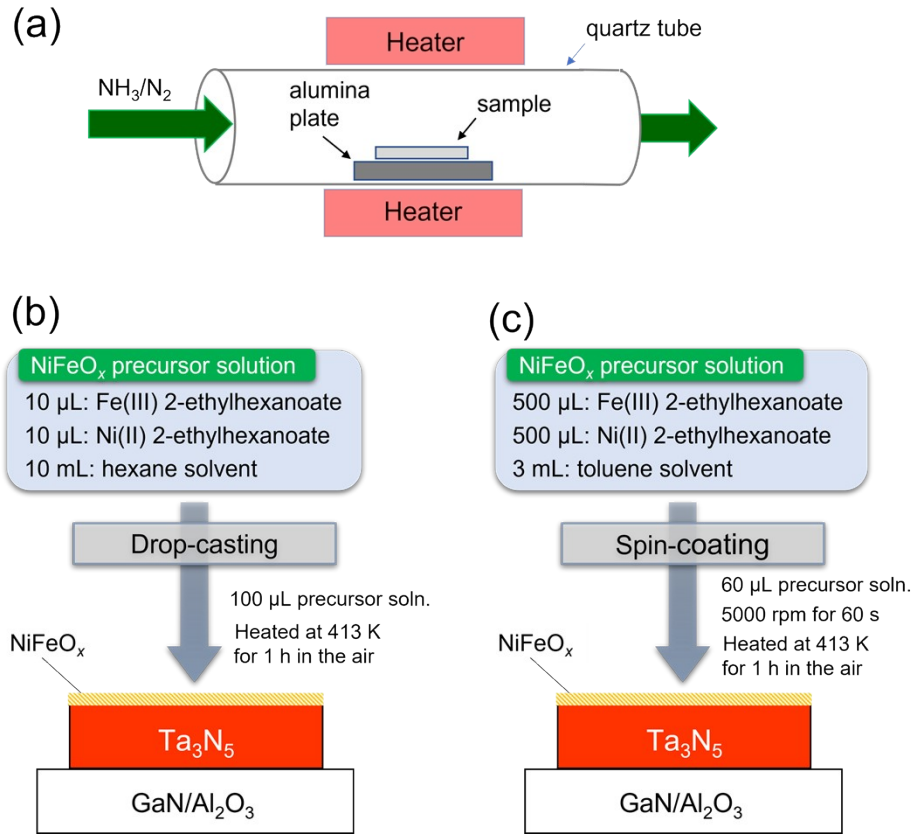


Figure S5. Fabrication processes of $NiFeO_x/Ta_3N_5/GaN/Al_2O_3$ photoanodes. (a) schematic depiction of nitridation furnace. (b, c) Surface modification with $NiFeO_x$ electrocatalyst using drop-casting and spin-coating methods and thermal heating on $Ta_3N_5/GaN/Al_2O_3$ sample.

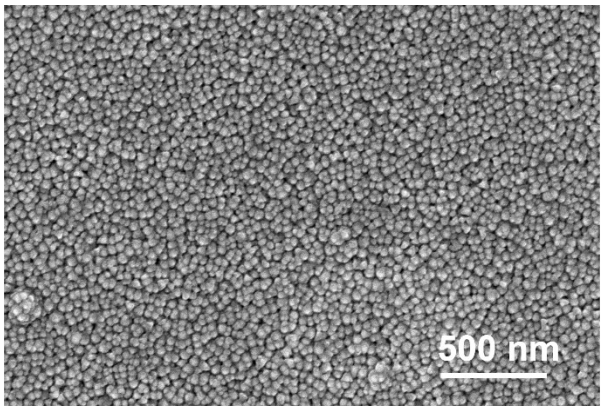


Figure S6. Scanning electron microscopy (SEM) image of $Ta_3N_5$ surface. The $Ta_3N_5$ thin film is fabricated on $GaN/Al_2O_3$ substrate by using high input power RF-MS and nitridation protocols.

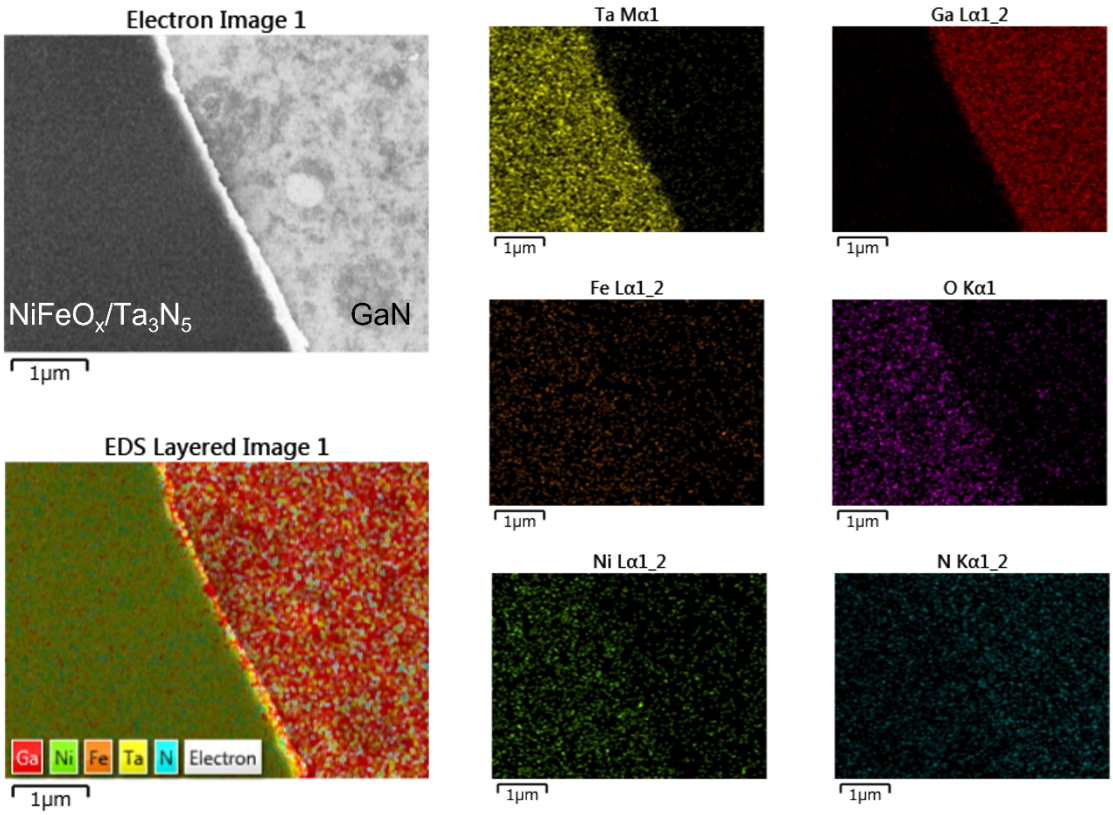


Figure S7. Scanning electron microscopy energy dispersive X-ray spectroscopy (SEM-EDS) mapping of $Ta_3N_5$/GaN/$Al_2O_3$ photoanode, modified with $NiFeO_x$ electrocatalyst loaded by spin-coating and thermal heating methods.

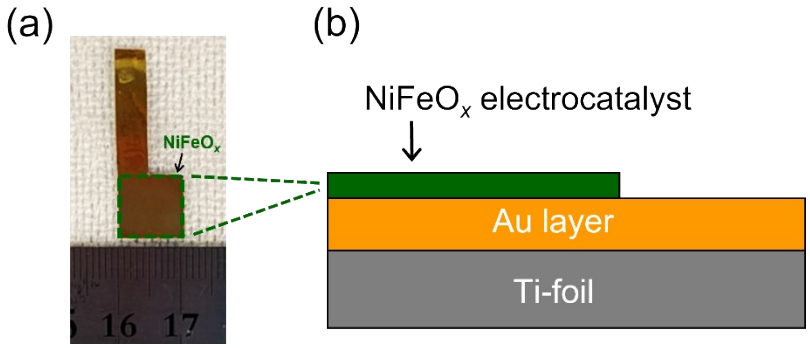


Figure S8. Surface modification of Au/Ti substrate with $NiFeO_x$ electrocatalyst. (a) Photograph (top view) and (b) schematic (side view) of the $NiFeO_x$/Au/Ti electrode.

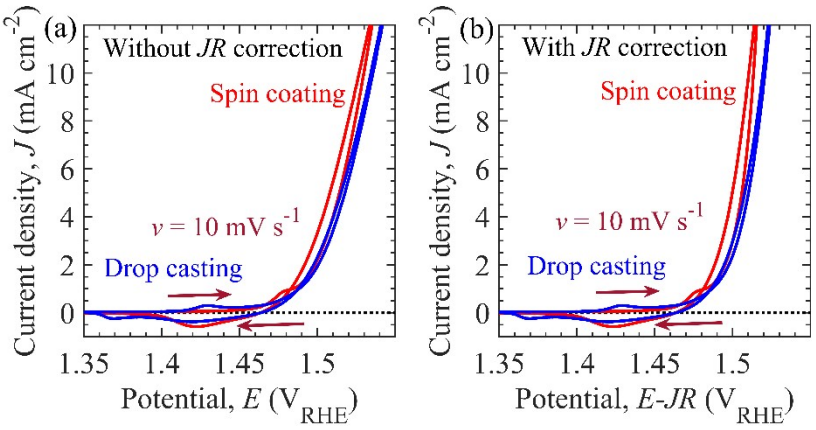


Figure S9. Electrochemical properties of $NiFeO_x$/Au/Ti electrode. Cyclic voltammograms (a) without and (b) with *iR*-drop correction of $NiFeO_x$/Au/Ti electrodes. Here, the *iR* drop is determined from AC impedance measurements. The electrodes are prepared by spin-coating and drop-casting methods with a loaded amount of 0.1 μmol $cm^{-2}$. The measurements are performed in 1.0 M KOH aqueous solution with pH = 13.9 and at the potential sweep rate of 10 mV $s^{-1}$.

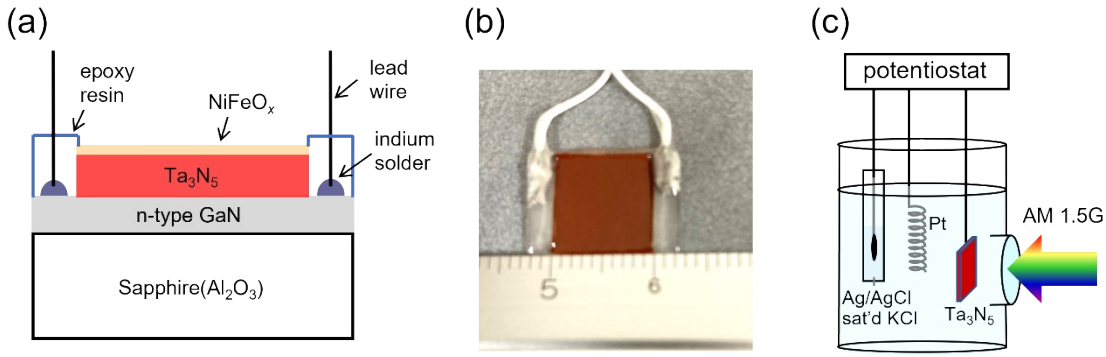


Figure S10. (a) Schematic (b) and photograph of $NiFeO_x/Ta_3N_5/GaN/Al_2O_3$ photoanode employed in a (c) three-electrode configuration for the PEC measurements.

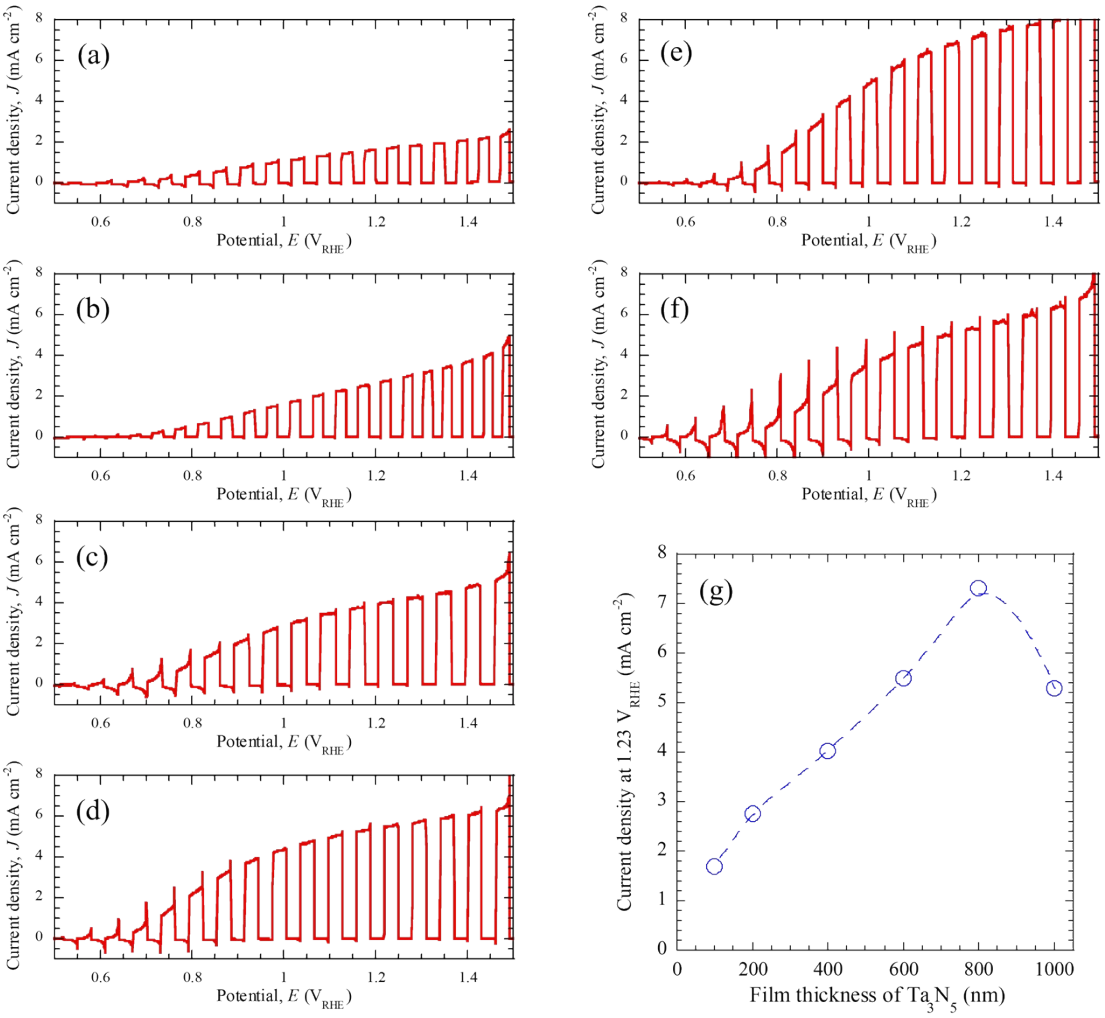


Figure S11. Impact of $Ta_3N_5$ film thickness on the performance characteristics $NiFeO_x/Ta_3N_5/GaN/Al_2O_3$ photoanodes in 1.0 M KOH aqueous solution. Current-potential (*J-E)* characteristics of photoanode at $Ta_3N_5$ film thickness of (a) 100 nm, (b) 200 nm, (c) 400 nm, (d) 600 nm, (e) 800 nm, and (f) 1000 nm. (g) Variation of current density *J* at 1.23 $V_{RHE}$ against film thickness of $Ta_3N_5$.The optimized film thickness of 800 nm is obtained to achieve high current density of 7.4 mA $cm^{-2}$.

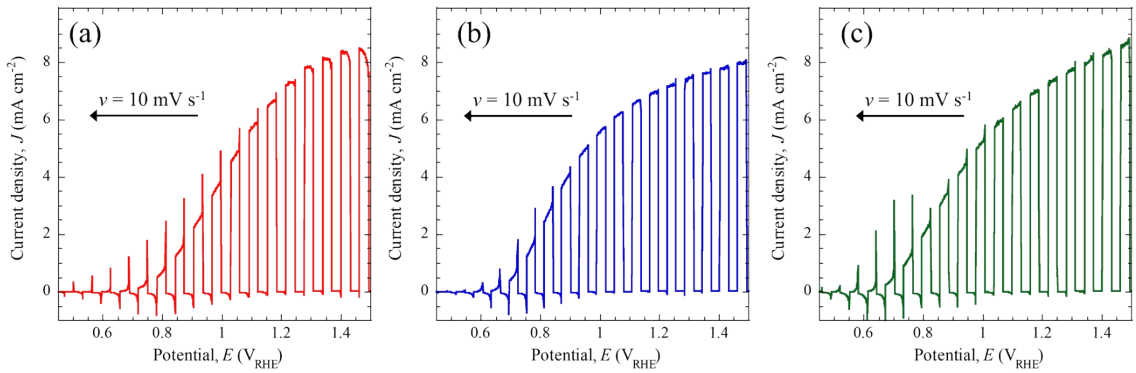


Figure S12. (a-c) Performance reproducibility of $NiFeO_x/Ta_3N_5/GaN/Al_2O_3$ photoanodes prepared by high-input-power RF-MS. The current potential (*J-E*) curves were obtained in 1.0 M KOH aqueous solution with pH 13.8 under chopped AM 1.5G solar illumination. The potential sweep rate ($v$) was set to 10 mV $s^{-1}$. An average photocurrent density of 7.37 ± 0.06 mA $cm^{-2}$ at 1.23 $V_{RHE}$ was obtained from five different samples.

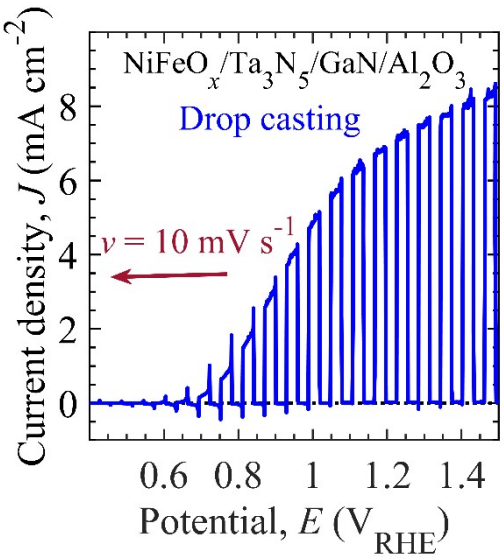


Figure S13. Photoelectrochemical characteristics of $NiFeO_x/Ta_3N_5/GaN/Al_2O_3$ photoanode. Current potential (*J-E*) curve of photoanode, prepared by drop-casting method. The data was acquired in 1 M KOH aqueous solution (pH = 13.8) under chopped simulated AM1.5G solar illumination. The intermittent period of light illumination and the potential sweep rate were 6 seconds and 10 mV $s^{-1}$, respectively.

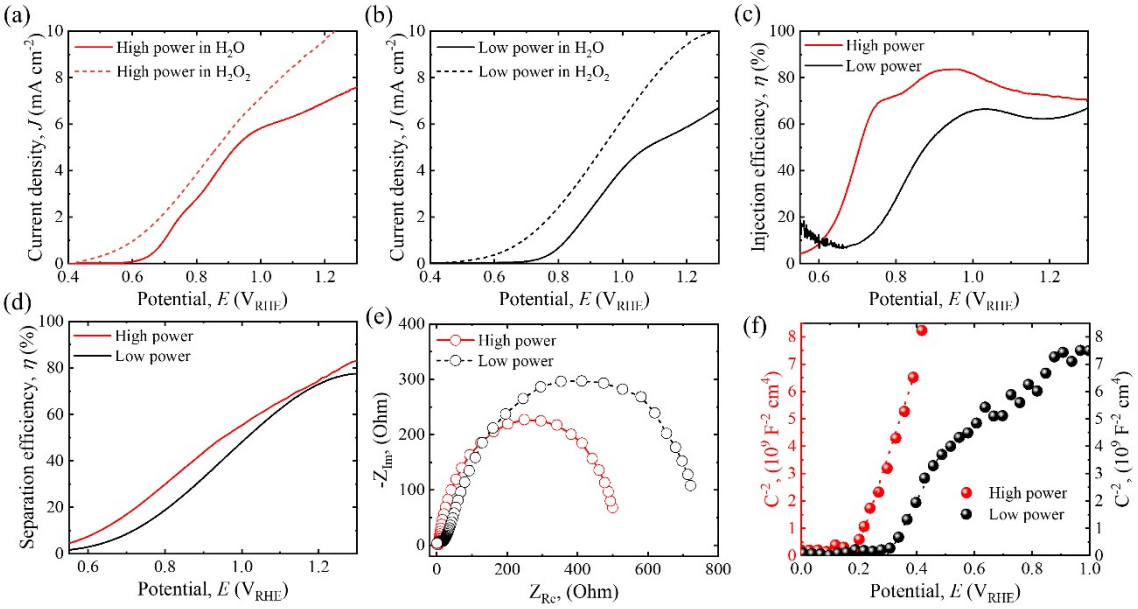


Figure S14. Photoelectrochemical characterization of the semitransparent $NiFeO_x/Ta_3N_5/GaN/Al_2O_3$ photoanodes. Current potential (*J-E*) curves of $Ta_3N_5$ photoanode, prepared by (a) high (optimized) and (b) low (non-optimized) power RF-MS technique. The measurements were performed in 1 M KOH (solid lines) and 1 M of KOH + 0.5 M $H_2O_2$ electrolyte (dashed lines) at pH 13.8 under simulated AM1.5G solar light. The *J-E* curves were recorded by sweeping potential from cathodic to anodic direction at a scan rate of 10 mV $s^{-1}$. Estimated (c) injection and (d) separation efficiencies of optimized (in red) and non-optimized (in black) photoanodes. (e) Nyquist plots of photoanodes measured under AM1.5G solar light at applied potential of 1.23 $V_{RHE}$. (f) Mott-Schottky analysis $1/C^2$ vs. $E$ ($C$ is measured capacitance at frequency of 5 kHz under dark condition) of the photoanodes. The dotted lines show the linear fits to determine flat band potential 0.19 $V_{RHE}$ and 0.31 $V_{RHE}$ of optimized and non-optimized photoanodes, respectively. Prior to measurements in panels (e, f), the electrolyte (with 1 M KOH and pH of 13.8) was purged by Ar gas for 15 min under stirring condition.

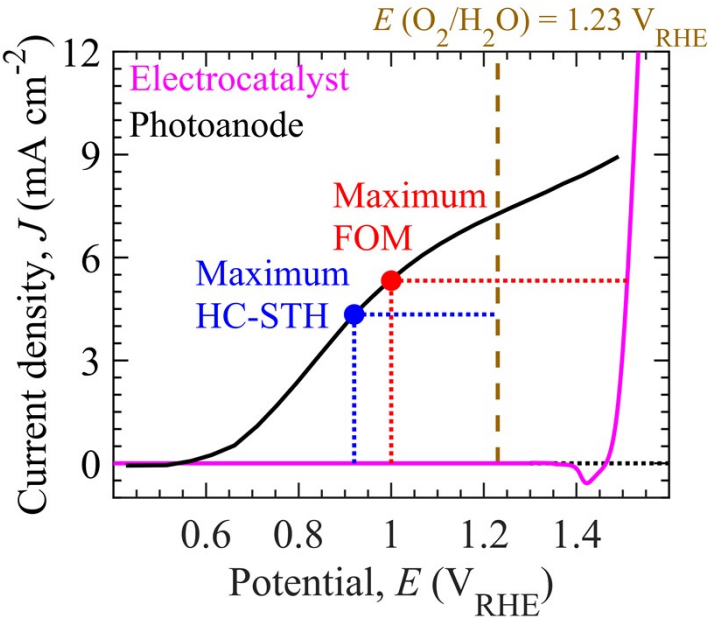


Figure S15. Determination of maximum half-cell solar-to-hydrogen (HC-STH) energy conversion efficiency (HC-STH) and the ratio-metric power-saved figure of merit (FOM) from photoelectrochemical and electrochemical measurements of $Ta_3N_5$-based photoanode and $NiFeO_x$/Au/Ti electrode, respectively. $E$ ($O_2/H_2O$) = 1.23 $V_{RHE}$ represents half-cell Nernst potential for the oxygen evolution reaction from solar water splitting. The maximum HC-STH and the FOM are 1.4 % at 0.9 $V_{RHE}$ and 2.7 % at 1.0 $V_{RHE}$, respectively.

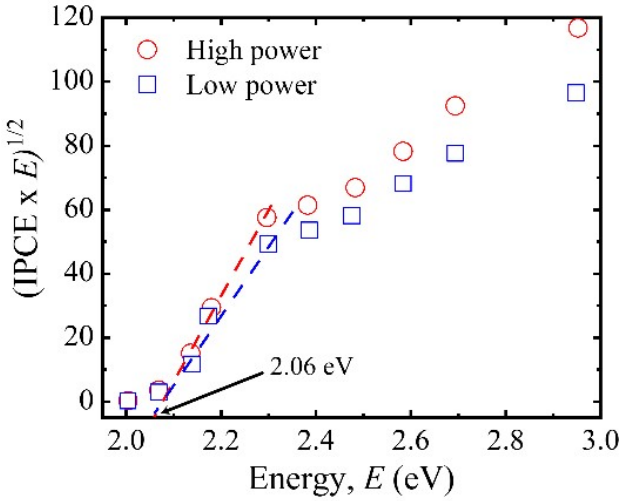


Figure S16. Tauc plots of $NiFeO_x/Ta_3N_5/GaN/Al_2O_3$ photoanodes prepared by high (optimized) and low (non-optimized) RF power sputtering process. The plots are derived from incident-photon-to-current efficiency (IPCE) spectra of respective photoanodes.

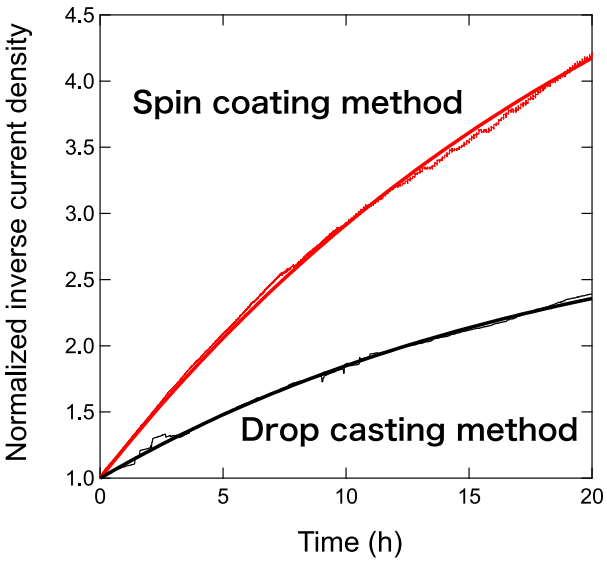


Figure S17. The normalized inverse current density $J_0/J(t)$ at 1.5 $V_{RHE}$ under the dark condition is shown against time. $J_0$=10.9 mA $cm^{-2}$ and 8.3 mA $cm^{-2}$ are obtained for spin-coating and drop-casting methods, respectively. The red curves and the black curves indicate $NiFeO_x$ electrocatalysts loaded with the spin-coating and drop-casting methods, respectively. The thin lines indicate the experimental data. The thick lines are the results of fit to Eq. S12. $r_{df}/r_{ci}$ are 6.58 for the spin-coating method and 3.11 for the drop-casting method. $k_{diss}J_0r_{ci}/r_{df}$ are 0.042 $h^{-1}$ for the spin-coating method and 0.051 $h^{-1}$ for the drop-casting method, respectively.

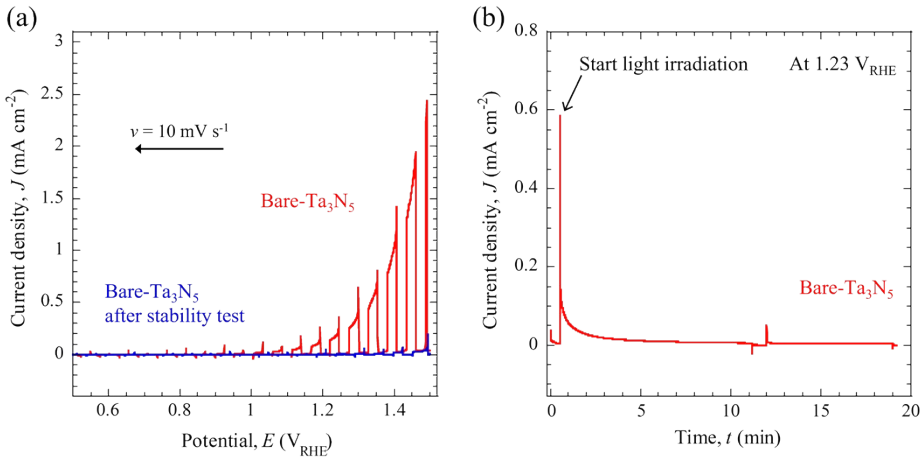


Figure S18. PEC performance of the bare $Ta_3N_5$ photoanode made by high input power RF-MS. (a) Current *versus* potential (*J*-*E*) curves of bare $Ta_3N_5$ photoanode before (red curve) and after (blue curve) stability test under chopped simulated AM1.5G solar light.

(b) Chronoamperometry characteristic of bare $Ta_3N_5$ photoanode at applied potential of 1.23 $V_{RHE}$ in 1M KOH electrolyte (pH = 13.8).

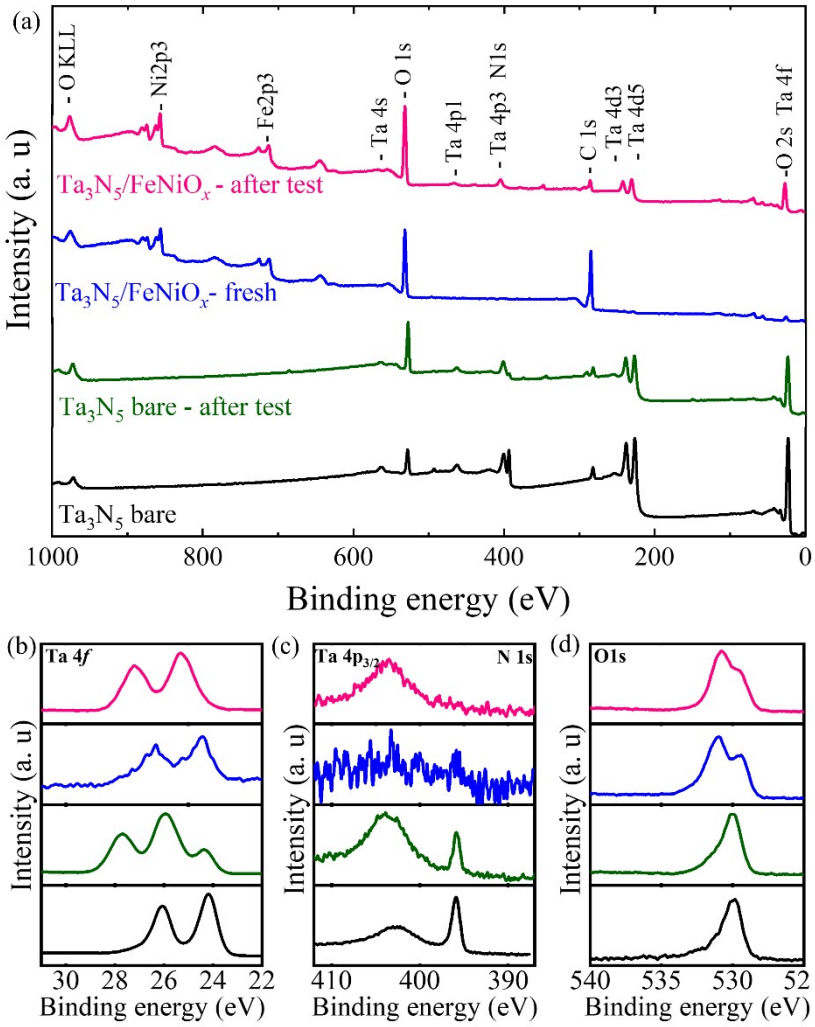


Figure S19. X-ray photoelectron spectroscopy (XPS) spectra of $Ta_3N_5$ photoanodes prepared by high input power RF-MS. (a) Overall XPS spectra and (b-d) high resolution XPS spectra of bare $Ta_3N_5$ and $NiFeO_x/Ta_3N_5$ photoanodes before and after stability test. Here, the $NiFeO_x$ electrocatalyst was deposited by spin-coating method for the preparation of $NiFeO_x/Ta_3N_5/GaN/Al_2O_3$ photoanode.

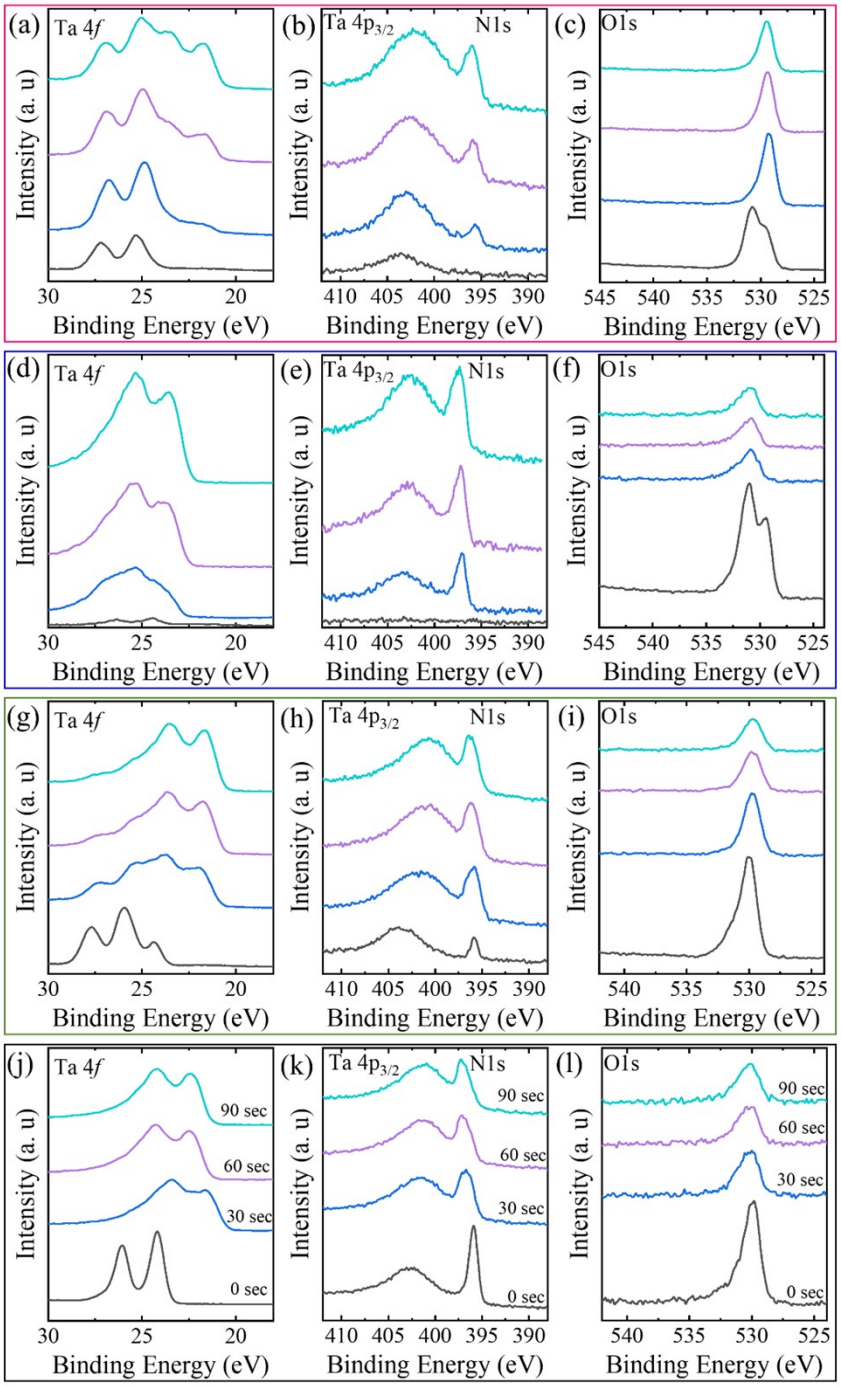


Figure S20. High resolution XPS spectra after Ar-etching treatment over 0 sec (in black), 30 sec (in blue), 60 sec (in purple), 90 sec (in emerald green) of $Ta_3N_5$ photoanodes. The panels (a-c), (d-f), (g-i), and (j-l) correspond to XPS spectra of $NiFeO_x/Ta_3N_5$ photoanode after stability test, $NiFeO_x/Ta_3N_5$ photoanode before stability test, bare $Ta_3N_5$ photoanode after stability test, and bare $Ta_3N_5$ photoanode before stability test, respectively.

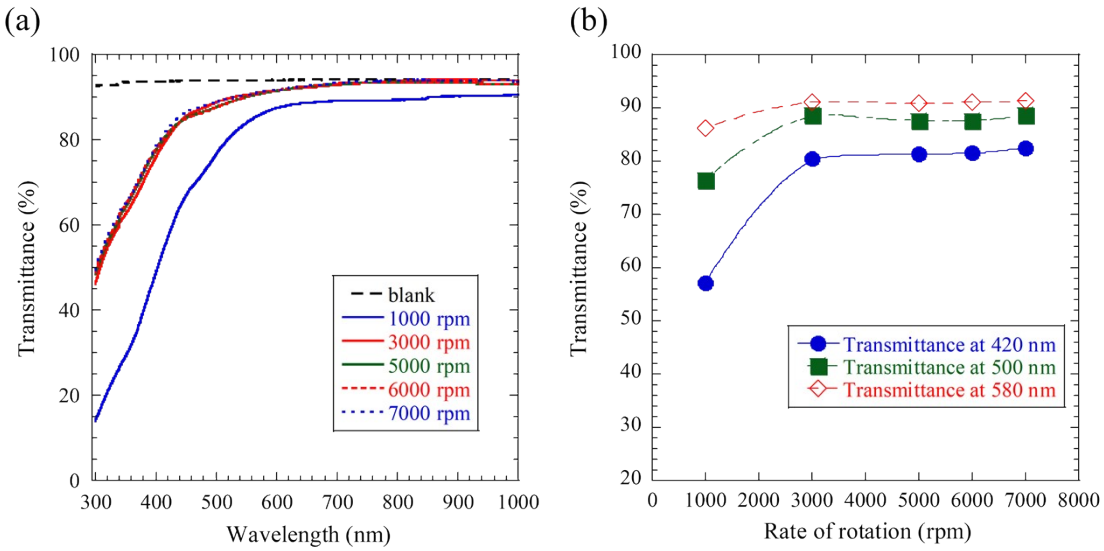


Figure S21. Influence of rotation speed on transmittance spectra of $NiFeO_x$ loaded quartz substrate. (a) UV-vis transmission spectra at various rotation speed (1000, 3000, 5000, 6000, and 7000 rpm). Here, the blank in legend correspond to bare quartz substrate without $NiFeO_x$. (b) Variation of transmittance with the rotation speed at wavelength of 420 nm, 500 nm, and 580 nm. The $NiFeO_x$ electrocatalyst was prepared by spin-coating methods by varying rotation speed. Here, the thickness of $NiFeO_x$ reduces with the increase of rotation speed.

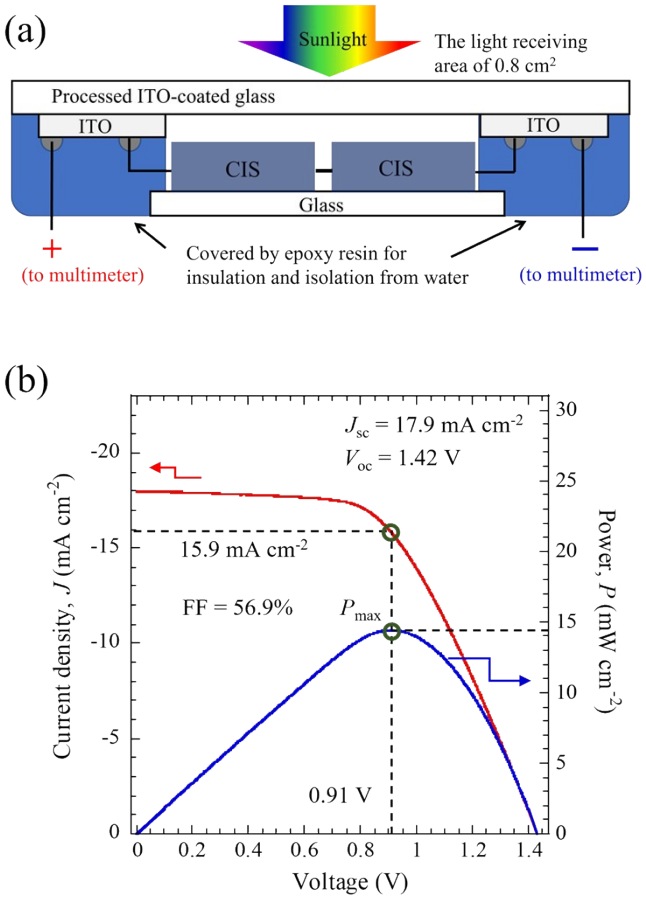


Figure S22. (a) Schematic depiction of cross-sectional dual-CIS element connected with processed ITO-coated glass. (b) Performance evaluation of two series connected dual-CIS. Current-voltage (on left axis; in red color) and power-voltage (on right axis; in blue color) characteristics of dual-CIS solar cell under continuous AM 1.5G solar illumination. The open-circuit voltage ($V_{oc}$), short-circuit current density ($J_{sc}$), fill factor (FF), and power conversion efficiency (PCE) (at maximum power point current of 15.9 mA cm$^{-2}$ at voltage 0.91 V) are 1.42 V, 17.9 mA cm$^{-2}$, 56.9 %, and 14.5 %, respectively.

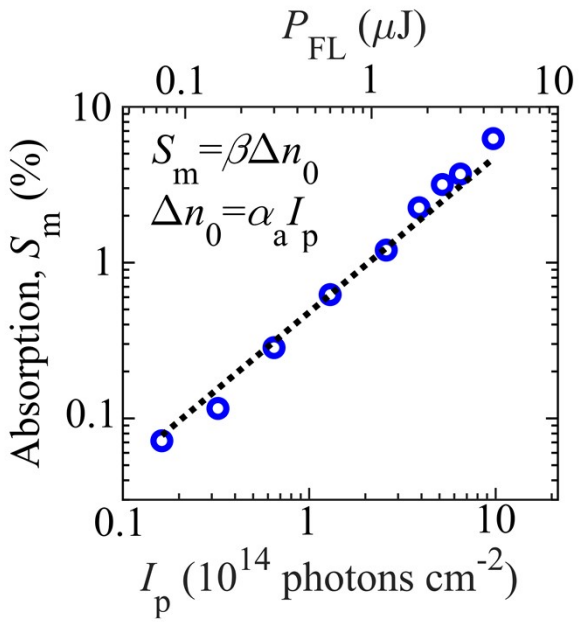


Figure S23. Variation of maximum absorption signal $S_m$ (at $t$ = 0.4 ps) against pump fluence intensity $P_{FL}$ and photon flux density $I_p$. The symbols and dotted line correspond to measured data (at $t$ = 0.4 ps) of Fig. 5b and relation $S_m = \beta \Delta n_0$ with $\beta$ = 1.65 × $10^{-20}$ $cm^3$, respectively. As per Lambert-Beer law, the $\Delta n_0$ = 1.88 × $10^{20}$ $cm^{-3}$ ($\alpha_a I_p$) is determined for absorption coefficient $\alpha_a$ = 2.91 × $10^{20}$ $cm^{-3}$ at pump photon energy of 3.1 eV and pump fluence intensity $P_{FL}$ of 3 μJ per pulse.

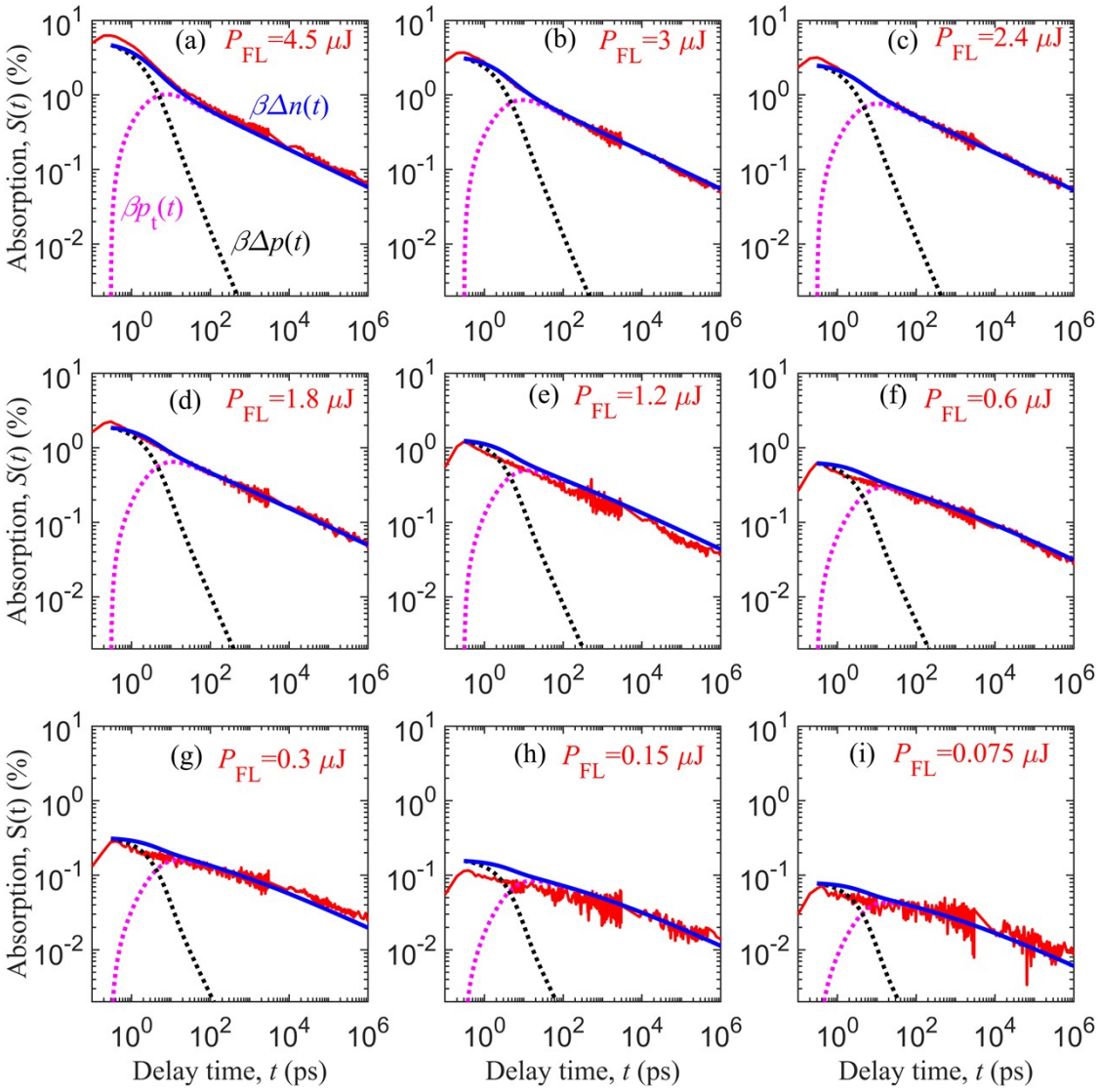


Figure S24. Charge carrier dynamics of $Ta_3N_5$ thin film prepared by high input power RF-MS. (a-i) Absorption signal $S(t)$ decay characteristics (in red) versus probe delay time t for pump fluence intensity $P_{FL}$ ranging from 0.075 μJ per pulse to 4.5 μJ per pulse. The pump and probe photon energy of 3.1 eV and 0.24 eV was utilized, respectively. The numerical simulation results are in reasonable agreement with the measured data for various $P_{FL}$.

**Table S4. Material parameters employed for theoretical simulations of charge carrier dynamics of $Ta_3N_5$ thin film.**

| Parameters, symbols | Estimated values |
|---|---|
| Effective density of states for conduction and valence bands, $N_{c,v}$ | $10^{20}$ cm$^{-3}$ (ref. 12) |
| Energy bandgap, $E_g$ | 2.108 eV [a] |
| Absorption coefficient, $a_a$ | $2.91 \times 10^5$ cm$^{-1}$ [b] |
| Initial photogenerated charge carrier density at $P_{FL}$ = 3μJ, $\Delta n_0$ | $1.88 \times 10^{20}$ cm$^{-3}$ [c] |
| Characteristic energy for exponential tail states, $E_0$ | 104 meV [d] |
| Doping density, $n_d$ | $8 \times 10^{19}$ cm$^{-3}$ [d] |
| Proportionality constant, $\beta$ | $1.65 \times 10^{-20}$ cm$^3$ [d] |
| Trap density, $N_t$ | $8.5 \times 10^{19}$ cm$^{-3}$ [d] |
| Recombination rate constant, $k_r$ | $10^{-9}$ cm$^3$s$^{-1}$ [d] |
| Trapping rate constant for holes, $k_t$ | $2 \times 10^{-9}$ cm$^3$s$^{-1}$ [d] |

[a] Determined from photoluminescence spectra in Fig. 5a.

[b] Estimated from ellipsometry measurements, provided by the authors of ref. [12, 35]

[c] Calculated in accordance with the Lambert-Beer law.

[d] Quantified from theoretical analysis of TAS measurements.

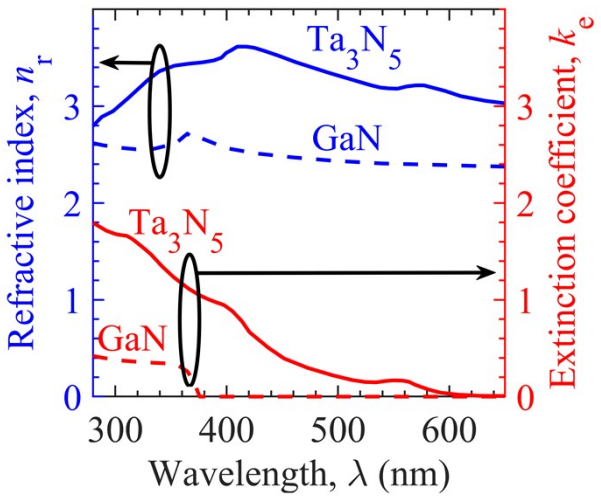


Figure S25. Refractive index and extinction coefficient of $Ta_3N_5$ and GaN layers for optical simulations of $Ta_3N_5$/GaN photoanode. The data is extracted from previous reports on $Ta_3N_5$ [35, 36] and online data base on GaN [37].

**Table S5. Estimated performance limiting parameters of $NiFeO_x/Ta_3N_5/GaN/Al_2O_3$ semitransparent photoanode.**

| Parameters, symbols | Estimated values |
|---|---|
| Carrier lifetime, $\tau = 1/k_r n_d$ | 12.5 ps |
| Hole diffusion length, $L_{dh} = (D\tau)^{0.5}$ * | 431 nm |
| Hole extraction rate at $Ta_3N_5$ surface, $S_h$ | 0.2 cm $s^{-1}$ |
| Series Resistance, $R_s$ | 59 Ω $cm^2$ |

* D is the diffusion constant

## References


1. J. Brillet, J. H. Yum, M. Cornuz, T. Hisatomi, R. Solarska, J. Augustynski, M. Graetzel and K. Sivula, *Nat. Photonics*, 2012, **6**, 824-828.
2. J. W. Jang, C. Du, Y. Ye, Y. Lin, X. Yao, J. Thorne, E. Liu, G. McMahon, J. Zhu, A. Javey, J. Guo and D. Wang, *Nat. Commun.*, 2015, **6**, 7447.
3. C. G. Morales-Guio, M. T. Mayer, A. Yella, S. D. Tilley, M. Grätzel and X. Hu, *J. Am. Chem. Soc.*, 2015, **137**, 9927-9936.
4. Gurudayal, D. Sabba, M. H. Kumar, L. H. Wong, J. Barber, M. Grätzel and N. Mathews, *Nano Lett.*, 2015, **15**, 3833-3839.
5. Gurudayal, R. A. John, P. P. Boix, C. Yi, C. Shi, M. C. Scott, S. A. Veldhuis, A. M. Minor, S. M. Zakeeruddin, L. H. Wong, M. Grätzel and N. Mathews, *ChemSusChem*, 2017, **10**, 2449-2456.
6. J. Park, K. Y. Yoon, T. Kim, H. Jang, M. J. Kwak, J. Y. Kim and J. H. Jang, *Nano Energy*, 2020, **76**, 105089.
7. W. J. Lee, P. S. Shinde, G. H. Go and E. Ramasamy, *Int. J. Hydrog. Energy*, 2011, **36**, 5262-5270.
8. F. F. Abdi, L. Han, A. H. M. Smets, M. Zeman, B. Dam and R. van de Krol, *Nat. Commun.*, 2013, **4**, 2195.
9. L. Han, F. F. Abdi, R. van de Krol, R. Liu, Z. Huang, H. J. Lewerenz, B. Dam, M. Zeman and A. H. M. Smets, *ChemSusChem*, 2014, **7**, 2832-2838.
10. D. Xue, M. Kan, X. Qian and Y. Zhao, *ACS Sustain. Chem. Eng.*, 2018, **6**, 16228-16234.
11. S. Wang, P. Chen, Y. Bai, J. H. Yun, G. Liu and L. Wang, *Adv. Mater.*, 2018, **30**, 1800486.
12. T. Higashi, H. Nishiyama, Y. Suzuki, Y. Sasaki, T. Hisatomi, M. Katayama, T.

Minegishi, K. Seki, T. Yamada and K. Domen, *Angew. Chem. Int. Ed.*, 2019, **58**, 2300-2304.

13. D. Akagi, Y. Kageshima, Y. Hashizume, S. Aoi, Y. Sasaki, H. Kaneko, T. Higashi, T. Hisatomi, M. Katayama, T. Minegishi, S. Noda and K. Domen, *ChemPhotoChem*, 2019, **3**, 521-524.
14. S. Y. Reece, J. A. Hamel, K. Sung, T. D. Jarvi, A. J. Esswein, J. J. H. Pijpers, D. G. Nocera, *Science*, 2011, **334**, 645-648.
15. E. Verlage, S. Hu, R. Liu, R. J. R. Jones, K. Sun, C. Xiang, N. S. Lewis, H. A. Atwater, *Energy Environ. Sci.*, 2015, **8**, 3166-3172.
16. M. M. May, H. J. Lewerenz, D. Lackner, F. Dimroth, T. Hannappel, *Nat. Commun.*, 2015, **6**, 8286.
17. S. Okamoto, M. Deguchi, S. Yotsuhashi, *J. Phys. Chem. C*, 2017, **121**, 1393-1398.
18. J. L. Young, M. A. Steiner, H. Döscher, R. M. France, J. A. Turner, T. G. Deutsch, *Nat. Energy*, 2017, **2**, 17028.
19. D. Kang, J. L. Young, H. Lim, W. E. Klein, H. Chen, Y. Xi, B. Gai, T. G. Deutsch, J. Yoon, *Nat. Energy*, 2017, **2**, 17043.
20. W. H. Cheng, M. H. Richter, M. M. May, J. Ohlmann, D. Lackner, F. Dimroth, T. Hannappel, H. A. Atwater, H. J. Lewerenz, *ACS Energy Lett.*, 2018, **3**, 1795-1800.
21. M. A. Steiner, C. D. Barraugh, C. W. Aldridge, I. B. Alvarez, D. J. Friedman, N. J. Ekins-Daukes, T. G. Deutsch and J. L. Young, *Sustain. Energy Fuels*, 2019, **3**, 2837-2844.
22. M. Ben-Naim, R. J. Britto, C. W. Aldridge, R. Mow, M. A. Steiner, A. C. Nielander, L. A. King, D. J. Friedman, T. G. Deutsch, J. L. Young, T. F. Jaramillo, *ACS Energy Lett.*, 2020, **5**, 2631-2640.
23. J. Ziegler, B. Kaiser, W. Jaegermann, F. Urbain, J. P. Becker, V. Smirnov, F. Finger, *ChemPhysChem*, 2014, **15**, 4026-4031.
24. J. Luo, Z. Li, S. Nishiwaki, M. Schreier, M. T. Mayer, P. Cendula, Y. H. Lee, K. Fu, A. Cao, M. K. Nazeeruddin, Y. E. Romanyuk, S. Buecheler, S. D. Tilley, L. H. Wong, A. N. Tiwari, M. Grätzel, *Adv. Energy Mater.*, 2015, **5**, 1501520.
25. P. Dias, M. Schreier, S. D. Tilley, J. Luo, J. Azevedo, L. Andrade, D. Bi, A. Hagfeldt, A. Mendes, M. Grätzel, M. T. Mayer, *Adv. Energy Mater.*, 2015, **5**, 1501537.
26. M. Kim, B. Lee, H. Ju, J. Y. Kim, J. Kim, S. W. Lee, *Adv. Mater.*, 2019, **31**, 1903316.
27. R. Fan, S. Cheng, G. Huang, Y. Wang, Y. Zhang, S. Vanka, G. A. Botton, Z. Mi, M. Shen, *J. Mater. Chem. A*, 2019, **7**, 2200-2209.

28. S. K. Karuturi, H. Shen, A. Sharma, F. J. Beck, P. Varadhan, T. Duong, P. R. Narangari, D. Zhang, Y. Wan, J. H. He, H. H. Tan, C. Jagadish, K. Catchpole, *Adv. Energy Mater.*, 2020, **10**, 2000772.
29. S. A. Lee, I. J. Park, J. W. Yang, J. Park, T. H. Lee, C. Kim, J. Moon, J. Y. Kim, H. W. Jang, *Cell Reports Phys. Sci.*, 2020, **1**, 100219.
30. T. Higashi, H. Nishiyama, Y. Otsuka, Y. Kawase, Y. Sasaki, M. Nakabayashi, M. Katayama, T. Minegishi, N. Shibata, K. Takanabe, T. Yamada and K. Domen, *ChemSusChem*, 2020, **13**, 1974-1978.
31. T. Higashi, Y. Sasaki, Y. Kawase, H. Nishiyama, M. Katayama, K. Takanabe and K. Domen, *Catalysts*, 2021, **11**, 584.
32. Y. Kawase, T. Higashi, K. Domen and K. Takanabe, *Adv. Energy Sustainability Res.*, 2021, **2**, 2100023.
33. J. K. A. Campa, M. Topic, *Prog. Electromagn. Res.*, 2013, **137**, 187-202.
34. K. K. N. Simon, M. Sze, *Physics of Semiconductor Devices*, John Wiley & Sons, Hoboken, NJ, 1981.
35. Y. Pihosh, T. Minegishi, V. Nandal, T. Higashi, M. Katayama, T. Yamada, Y. Sasaki, K. Seki, Y. Suzuki, M. Nakabayashi, M. Sugiyama and K. Domen, *Energy Environ. Sci.*, 2020, **13**, 1519-1530.
36. V. Nandal, Y. Pihosh, T. Higashi, T. Minegishi, T. Yamada, K. Seki, M. Sugiyama and K. Domen, *Energy Environ. Sci.*, 2021, **14**, 4038-4047.
37. A. K. C. FILMETRICS, Refractive Index of GaN, Gallium Nitride, https://www.filmetrics.com/refractive-index-database/GaN/Gallium-Nitride#:~:text=For%20a%20typical%20sample%20of,nm%20are%202.37966%20and%200).